A druggable addiction to *de novo* pyrimidine biosynthesis in diffuse midline glioma

Sharmistha Pal[1], Jakub P. Kaplan[1], Huy Nguyen[1], Sylwia A. Stopka[2,3], Michael S. Regan[2], Quang-De Nguyen[4], Kristen L. Jones[4], Lisa A. Moreau[1,5], Andrew Perciaccante[2], Bradley Hunsel[1], Kevin X. Liu[10], Jingyu Peng[6], Mariella G. Filbin[7], Nathalie Y.R. Agar[2,3,8], Dipanjan Chowdhury[1,9], and Daphne Haas-Kogan[10, 11,*]

[1]Department of Radiation Oncology, Dana-Farber Cancer Institute, Boston, Massachusetts, 02215, United States
[2]Department of Neurosurgery, Brigham and Women's Hospital, Harvard Medical School, Boston, Massachusetts, 02215, United States
[3]Department of Radiology, Brigham and Women's Hospital, Harvard Medical School, Boston, Massachusetts, 02215, United States
[4]Center for Biomedical Imaging in Oncology, Dana-Farber Cancer Institute, Boston, Massachusetts, 02210, United States
[5]Center for DNA Damage and Repair, Dana-Farber Cancer Institute, Boston, Massachusetts, 02215, United States
[6]Division of Molecular and Cellular Oncology, Dana-Farber Cancer Institute, Boston, Massachusetts, 02215, United States
[7]Department of Pediatric Oncology, Dana-Farber Boston Children's Cancer and Blood Disorders Center, Boston, MA 02115, USA
[8]Department of Cancer Biology, Dana-Farber Cancer Institute, Boston, Massachusetts, 02215, United States
[9]Department of Biological Chemistry & Molecular Pharmacology, Harvard Medical School, Boston, MA 02115, USA; Broad Institute of Harvard and MIT, Cambridge, Massachusetts, 02142, United States
[10]Department of Radiation Oncology, Brigham and Women's Hospital, Dana-Farber Cancer Institute, Boston Children's Hospital, Harvard Medical School, Boston, Massachusetts, 02215, United States

[11]Lead author
*Correspondence: dhaas-kogan@bwh.harvard.edu

SUMMARY

Diffuse midline glioma (DMG) is a uniformly fatal pediatric cancer driven by oncohistones that do not readily lend themselves to drug development. To identify therapeutic targets for DMG, we conducted a genome-wide CRIPSR screen for DMG metabolic vulnerabilities, which revealed a DMG selective dependency on the *de novo* pathway for pyrimidine biosynthesis. The dependency is specific to pyrimidines as there is no selectivity for suppression of *de novo* purine biosynthesis. A clinical stage inhibitor of DHODH (a rate limiting enzyme in the *de novo* pathway) generates DNA damage and induces apoptosis through suppression of replication forks--an “on target” effect, as shown by uridine rescue. MALDI mass spectroscopy imaging demonstrates that BAY2402234 accumulates in brain at therapeutically relevant concentrations, suppresses *de novo* pyrimidine biosynthesis *in vivo,* and prolongs survival of mice bearing intracranial DMG xenografts. Our results highlight BAY2402234, a brain-penetrant DHODH inhibitor, as a promising therapy against DMGs.

KEYWORDS: diffuse midline glioma, diffuse intrinsic pontine glioma, DHODH, *de novo* pyrimidine synthesis, ATR, replication stress, BAY2402234, elimusertib

INTRODUCTION

Diffuse midline glioma (DMG), hitherto known as diffuse intrinsic pontine glioma (DIPG), is a class of high-grade glioma that develops in the midline structures of the brain. DMGs occur mostly in children (median age of 6-7 years), and less frequently in young adults. These malignant and universally fatal gliomas are not amenable to surgical resection due to the tumor site and their diffuse and infiltrative growth. Moreover, no chemotherapeutic, biological, or any other systemic agent has proven effective against DMGs. Radiotherapy prolongs survival of most patients, but tumor progression and death are inevitable. With median survival of less than a year, DMGs are the leading cause of brain cancer deaths in children (Braunstein et al., 2017; Cooney et al., 2017; Jones et al., 2017; Ostrom et al., 2017; Sturm et al., 2017).

Unlike most other pediatric cancers for which immense progress has been made in identifying efficacious novel treatments and improving patient outcomes, survival for DMGs has not changed in over 50 years. Given the failure of conventional therapeutic modalities, considerable effort has been devoted to development of targeted therapeutics. Seminal work over the last decade has identified the prevalent oncogenic drivers of DMG as a set of recurrent amino acid substitution mutations in histone H3.3 (*H3F3A*) and H3.1 (*HIST1H3B* and *HIST1H3C*) (Buczkowicz et al., 2014; Khuong-Quang et al., 2012; Wu et al., 2012). Of these, the H3K27M amino acid substitution is the most common (80%) leading to the designation, “H3K27M mutant diffuse midline glioma (DMG)” by the World Health Organization. The outcome of this single amino acid substitution is a genome-wide reconfiguration of chromatin architecture via loss of repressive H3K27 trimethylation (Bender et al., 2013; Harutyunyan et al., 2019; Wu et al., 2012). A subset of DMGs contain mutations in other effectors of chromatin architecture. In particular, EZHIP overexpression has been described as a second route towards loss of H3K27 trimethylation in a subset of those DMGs lacking H3K27M mutations (Castel et al., 2020).

Unfortunately, while H3K27M is a key driver in DMG, the mutated histone H3 has no enzymatic function and thus does not lend itself to development of small molecule antagonists (Bender et al., 2013; Krug et al., 2019; Larson et al., 2019; Nagaraja et al., 2019; Silveira et al., 2019). Various work-arounds, including histone deacetylase (HDAC) inhibitors, are being developed but have yet to show any benefit for DMG patients. For example, the HDAC inhibitor panobinostat, identified in a drug screen, counteracts epigenetic dysregulation and restores H3K27 trimethylation but poses a challenge for clinical use due to its inability to cross the BBB (Nagaraja et al., 2017). Besides epigenetic alterations, other common alterations in DMGs include inactivation of the TP53 pathway, activation of PI3K, PDGF or ACVR1 signaling, and dysregulation of G1-S cell cycle checkpoint (Mackay et al., 2017). Attempts to target these signaling pathways have yet to show any clinical benefit.

Against this backdrop, an emerging body of data shows that tumor cells adapt to the stresses created by oncogenic driver mutations (Luo et al., 2009; Pagliarini et al., 2015). These adaptations can create vulnerabilities to otherwise innocuous inhibitors of common metabolic pathways. To explore this route towards a targeted therapeutic for DMG, we conducted an unbiased, CRISPR-based screen for DMG-specific vulnerabilities. The screen identified a druggable addiction to the *de novo* pathway for pyrimidine biosynthesis. Studies summarized herein describe a clinical stage, brain penetrant small molecule inhibitor of this pathway and show that this drug (BAY2402234) selectively kills DMG cells *in vitro* and *in vivo* via induction of replication stress-mediated DNA damage. Of interest, a manuscript by Shi et al which has been co-submitted, reports similar findings for IDH-mutant glioma--another aggressive glioma of young people wherein the primary oncogenic driver, like H3K27M mutant histone, has no intrinsic mitogenic function but rather serves to reconfigure tumor cell chromatin.

RESULTS

A genome-wide CRISPR loss-of-function screen for DMG vulnerabilities

To uncover intrinsic vulnerabilities of DMGs, we performed a genome-wide CRISPR-based dependency screen in three distinct DMG cell lines to identify genes whose loss would lead to DMG cell death (Figure S1). As expected, the genes that were identified as required for DMG cell viability encompassed pan-cancer essential genes (Tables S1 and S2) that were excluded from further analysis. A Venn diagram depicting overlap among the remaining genes (henceforth referred to as DMG dependency genes, Table S3) in the three DMG lines revealed 213 genes shared between at least two cell lines but only 13 dependency genes common to all three DMG lines (Figure 1A). We performed Ingenuity pathway analysis (IPA) on the 213 genes shared by at least two of the cell lines and found that the top five biological pathways defined by these dependency genes (Figure 1B) are associated with metabolism and DNA damage repair. We chose to focus on uridine-5'-phosphate (UMP) biosynthesis because every component of this pathway was among the DMG dependency genes. Specifically, all three genes that execute *de novo* pyrimidine biosynthesis [carbamoyl-phosphate synthetase 2, aspartate transcarbamylase, dihydroorotase, (*CAD*); dihydroorotate dehydrogenase (*DHODH*); uridine monophosphate synthetase (*UMPS*)] to produce UMP, the precursor for all pyrimidine nucleotides, were identified in our screen as DMG dependencies (Figure 1C). We validated this DMG dependency on *de novo* pyrimidine synthesis using shRNA to knockdown expression of *CAD* and *DHODH* and found that knockdown of either *CAD* or *DHODH* inhibited proliferation in all three DMG cells tested (Figures 1D and S2).

De novo pyrimidine biosynthesis as a druggable DMG vulnerability

BAY2402234 is a clinical stage, small molecule inhibitor of DHODH. We evaluated the impact of BAY2402234 on DMG growth using a panel of patient-derived cell lines that included H3 wild-type (DIPG1), H3.1K27M mutant (SU-DIPG4, SU-DIPG21, SU-DIPG33, SU-DIPG36), and

H3.3K27M mutant (BT869, SU-DIPG13, SU-DIPG17, CCHMC-DIPG2/DIPG2, HSJD-DIPG007) lines. We asked whether dependency on *de novo* pyrimidine biosynthesis was DMG-specific or more broadly applicable to high-grade gliomas, and therefore tested the effects of BAY2402234 against DMGs as well as adult glioblastomas (aGBM) and normal immortalized human astrocytes. We found that all tested DMG cell lines were exquisitely sensitive to growth inhibition by BAY2402234 (IC50<1nM) relative to the aGBMs and astrocytes (Figure 2A). Furthermore, we observed no correlation between proliferation rate and sensitivity to BAY2402234 indicating that DMG-specific sensitivity to DHODH inhibition was not proliferation-related (Figure S3).

To validate *de novo* pyrimidine synthesis as the BAY2402234 target, we quantified pathway metabolites in cells treated with BAY2402234 using matrix-assisted laser desorption/ionization (MALDI) mass spectroscopy. Twenty-four hours after treatment with BAY2402234, metabolites that are specific to *de novo* pyrimidine synthesis and lie upstream of DHODH (N-carbamoyl-L-aspartate and dihydroorotate), accumulated in treated cells (Figures 2B and S4A). In contrast, the pathway end-product, UMP, downstream of DHODH was depleted in BAY2402234-treated DMG cells, indicating on-target inhibition of *de novo* pyrimidine synthesis by the drug (Figures 2B and S4B). Consistent with the hypersensitivity of DMG to BAY2402234, we observed more pronounced BAY2402234-induced depletion of UMP pools in DMG, indicating greater dependence of DMGs on the *de novo* pathway to maintain cellular pyrimidine nucleotides (Figure S4B).

To confirm that growth inhibition of DMGs is an on-target response to suppression of *de novo* rather than salvage pyrimidine biosynthesis by BAY2402234, we asked whether exogenous uridine would fully rescue BAY2402234-induced growth inhibition. Validation by uridine rescue is possible because pyrimidine nucleotides can by synthesized by either the *de novo* or salvage pathway, but uridine supplementation specifically rescues inhibition of the former pathway by replenishing UMP pools. As shown in Figure 3A, exogenous uridine completely rescued the dose-dependent effects of BAY2402234 on cell growth, confirming the

on-target mechanism of *de novo* pyrimidine synthesis pathway inhibition in DMG. In contrast to DMGs, exogenous uridine had no impact on proliferation of aGBMs or normal human astrocytes. The essential roles of pyrimidines in DNA replication and repair led us to evaluate drug-induced DNA damage levels by quantifying γ-H2AX, a marker for DNA damage. Following BAY2402234 treatment, we documented a 2-4-fold increases in γ-H2AX-positive DMG cells, and this induction of DNA damage was completely rescued by uridine supplementation (Figure 3B).

We show above that DMGs are dependent on *de novo* pyrimidine biosynthesis; but we wanted to confirm that this dependency was specific to pyrimidines and not more broadly applicable to *de novo* nucleotide synthesis. To this end, we used VX-497, a small molecule inhibitor of IMPDH, which blocks *de novo* purine, specifically GMP synthesis, but not pyrimidine synthesis (Figure 4A). IC50 values for VX-497 in DMG cells were approximately 2000-fold higher than IC50 values for BAY2402234 and unlike BAY2402234, VX-497 did not result in differential sensitivity of DMGs compared to aGBMs. Similarly, no unique, pronounced sensitivity was observed in DMGs when treated with chemotherapy agents, fluoropyrimidine 5-fluorouracil (5-FU), gemcitabine, and hydroxyurea, which all interfere with nucleotide synthesis and/or DNA replication (Figures 4B-D).

Having established the specific dependency of DMGs on *de novo* pyrimidine synthesis, we sought to understand the underlying mechanism for this vulnerability. We asked whether this dependency was due to differential expression of genes responsible for pyrimidine homeostasis, including *de novo* or salvage pyrimidine synthesis, and pyrimidine degradation. If gene expression differences underlay unique DMG sensitivity to DHODH inhibition, one would expect higher *de novo* gene expression or lower salvage pathway gene expression in DMGs relative to aGBMs. Elevated expression of pyrimidine degradation genes could also contribute to the DMG phenotype since degradation of pyrimidines would reduce available substrate for

the salvage pathway. Figure 4E shows that differences in expression of genes responsible for pyrimidine synthesis do not explain the reliance on *de novo* pyrimidine synthesis in DMGs compared to aGBMs (Figure 4E); however, increased expression of pyrimidine degradation genes is consistent with heightened DMG sensitivity to BAY2402234 (Figure 4E). To assess the contribution of increased pyrimidine degradation gene expression to DMG sensitivity to DHODH inhibition, we inhibited the enzyme that catalyzes the first step in uracil degradation, DPYD. Inhibition of DPYD using gimeracil partially rescued DMG hyper-sensitivity to BAY2402234 (Figure 4F). Taken together, we infer that DMG cells are reliant on the *de novo* pathway for pyrimidine biosynthesis and this vulnerability can be targeted with small molecule inhibitors of DHODH to induce cell death. Further, elevated expression of pyrimidine degradation genes is a mechanism of hyper-sensitivity of DMGs to DHODH inhibition. However, this mechanism does not fully account for the exquisite sensitivity seen in all DMGs.

DHODH inhibition arrests cell cycle progression, leads to replication stress, and induces apoptosis in DMG cells

As DMG-specific hyper-sensitivity to DHODH inhibition is accompanied by profound UMP depletion (Figure 2B), we hypothesized that multiple cell functions that rely on pyrimidine nucleotides would be affected by BAY2402234 treatment. Accordingly, we investigated BAY2402234's effects on cell cycle progression, replication, and induction of apoptosis (Figure 5). BAY2402234 induced accumulation of DMG cells in S-phase, as indicated by BrdU uptake (Figure 5A). Given the documented accumulation in S-phase we asked whether BAY2402234 caused replication stress in DMG cells. To address this question, we measured DNA-bound RPA, a known indicator of replication stress. As a positive control we use treatment with hydroxyurea (HU), which depletes cellular dNTP pools and is known to induce replication stress. As shown (Figure 5B), we observe increased RPA foci after treatment with HU. We

also documented increased RPA foci in BAY2402234-treated DMG cells, and this was completely rescued by exogenous uridine (Figure 5B).

The presence of DNA-bound RPA activates ATR, which phosphorylates both RPA2 at serine 33 (S33), and the downstream effector CHK1 at serine 345 (S345). To confirm ATR activation after DHODH inhibition, we examined phosphorylation of RPA2 and CHK1 by Western blot analysis. We observed induction of phosphorylation at RPA2^{S33} and CHK1^{S345} after BAY2402234 or HU treatment (Figure 5C). Consistent with our previous findings, induction of replication stress and ATR activation were associated with increased levels of γ-H2AX and cleaved PARP, indicating increased DNA damage. Uridine replenishment rescued the BAY2402234-induced effects on RPA/CHK1 and DNA damage (Figure 5C), indicating the specificity of the drug and confirming that *de novo* pyrimidine biosynthesis mediates the phenotype. To further confirm actual stalling of replication forks we directly evaluated replication fork progression in BAY2402234-treated DMGs using the DNA fiber combing assay. We observed that DHODH inhibition significantly decreased replication fork speed as indicated by smaller tracks of incorporated CldU and IdU (dUTP analog) after BAY2402234 treatment. Again, these findings were entirely reversed by uridine supplementation, as reflected in normal replication fork progression in DMGs treated with BAY2402234 in the presence of exogenous uridine (Figure 5D). Finally, we measured levels of cleaved CASPASE3, an apoptosis marker, after drug treatment. As indicated in Figure 5E, BAY2402234 causes an increase in the levels of cleaved CASPASE3. This increase was completely rescued by uridine supplementation indicating that the cellular mechanism of BAY2402234 on DMG growth (see Figure 2) reflects drug-induced apoptotic death. Taken together, our data indicate that DHODH inhibition may prove efficacious against DMGs by impeding *de novo* pyrimidine biosynthesis, thus causing replication stress, DNA damage, and cell death.

Inhibition of *de novo* pyrimidine biosynthesis by BAY2402234 prolongs survival of mice harboring DMG orthotopic tumors.

Having demonstrated promising anti-tumor activity *in vitro*, we asked whether BAY2402234 crossed the BBB and accumulated in intracranial DMG xenografts in mice brainstems. For this purpose, we implanted a luciferized DMG cell line (SU-DIPG13P*) (Nagaraja et al., 2017) into the brainstem (pons) of mice to establish intracranial DMG xenografts and then administered BAY2402234 by oral gavage. After four days of treatment, brain tissues were collected for analysis using matrix-assisted laser desorption ionization mass spectrometry imaging (MALDI-MSI). MALDI-MSI documented accumulation of BAY2402234 in intracranial pontine DMGs (Figures 6A and S5). To document the drug's target engagement and *in vivo* biochemical activity, we also quantified intra-tumoral levels of *de novo* pyrimidine synthesis pathway metabolites upstream and downstream of DHODH. Following treatment with BAY2402234, N-carbamoyl-L-aspartate and dihydroorotate, which lie upstream of DHODH, accumulated, whereas UMP, which lies downstream of DHODH, diminished throughout the pontine tumors, compared to vehicle-treated mice (Figures 6A-B, and S5D). As additional pharmacodynamic endpoints we measured DNA damage by γ-H2AX immunostaining and observed induction of DNA damage in BAY2402234-treated pontine DMGs (Figures 6C). All the *in vivo* pharmacodynamic results were consistent with our *in vitro* findings.

We next asked whether BAY2402234 would prolong survival of mice bearing DMG intracranial xenografts. Towards this end, we used two DMG xenograft models; one was a highly aggressive cell line (DIPG1) with median survival of untreated mice of ~7 days and the second was the SU-DIPG13-P* line which is moderately aggressive (median survival of untreated mice ~45 days). BAY2402234 treatment significantly decreased tumor burden as measured by bioluminescence signals (Figures 6D and S6A). In accordance, harvested tumor sections after BAY2402234 treatment displayed reduced Ki-67 positive tumor cells relative to vehicle treated tumors (Figure 6E). Finally, BAY2402234 administration prolonged survival of

mice in both the highly and the moderately aggressive DMG models (Figures 6F and S6B). Taken together, our data demonstrate that BAY2402234 crosses the BBB, accumulates in brainstem tumors *in vivo,* inhibits *de novo* pyrimidine biosynthesis leading to DNA damage and ultimately reduces tumor growth and prolongs survival of DMG-bearing mice.

Synergistic anti-cancer effects of DHODH- and ATR-inhibition in DMGs

We showed above that DHODH inhibition results in activation of ATR, a key kinase that is critical for mediating the DNA damage response induced by replication stress (Saldivar et al., 2017). We therefore hypothesized that adding ATR- to DHODH-inhibition would result in synergistic cytotoxicity in DMG cells. To test this hypothesis, we treated DMG cells with BAY2402234, elimusertib, or a combination thereof. We first asked whether the combination treatment would enhance replication stress and DNA damage more than either monotherapy. In all DMG lines, the combination of DHODH- and ATR-inhibition dramatically augmented RPA foci formation, replication stress, and induction of DNA damage (Figures 7A-B and S7A-C) compared with either monotherapy. Figure 7B shows that elimusertib effectively inhibits ATR signaling, reflected in loss of $RPA2^{S33}$ and $CHK1^{S345}$ phosphorylation. This Western blot further confirms enhanced DNA damage (γ-H2AX) and PARP cleavage resulting from combination therapy (Figure 7B) relative to either treatment alone. To confirm that elimusertib specifically inhibits ATR-mediated phosphorylation events, we examined an RPA site, T21, that is phosphorylated in response to replication stress in an ATR-independent fashion. We show that RPA^{T21} is phosphorylated after treatment with BAY2402234 or HU, a phosphorylation that persists even in the presence of elimusertib (Figure S7D).

Next, we asked whether replication stress induced by DHODH inhibition is reversible. DMG cultures were treated with BAY2402234 for 24 hours. The drug was then removed, and cells were cultured for an additional 24 hours. We monitored DNA damage by γ-H2AX

expression immediately before and after the 24-hour drug recovery period (Figure 8A). We observed that the limited DNA damage induced by BAY2402234 or elimusertib monotherapy was partially reversible. In contrast, the considerable levels of DNA damage induced by 24 hours of combination treatment proved irreversible in approximately 50% of cells, suggesting replication fork collapse.

We sought to quantitate the degree of chromosome/chromatid aberrations that resulted from either monotherapy or combination treatment. Cells were allowed to progress into mitosis and then captured at metaphase using colcemid. Analysis of metaphase spreads disclosed chromosome/chromatid aberrations in 29% after DHODH inhibition, 48% after ATR inhibition, and 76% after combined DHODH and ATR inhibition (Figure 8B).

The marked induction of replication stress, DNA damage, and chromosome/chromatid aberrations suggested that combined inhibition of DHODH and ATR would also lead to synergistic cell death. We tested this prediction using the Combenefit software to analyze monotherapy and combination treatments of DMG cultures. We found synergistic DMG cell killing by combined BAY2402234 and elimusertib therapy (Figure 8C). The marked synergy seen with BAY2402234 and elimusertib combination treatment confirms replication stress as a mechanism of cell death induced by DHODH inhibition.

DISCUSSION

DMGs are a uniformly fatal pediatric glioma, with only radiotherapy as a treatment modality that alleviates symptoms and prolongs survival and no effective systemic agents. DMGs are driven by amino acid substitution mutants of histone H3. The mutant histones function to reconfigure chromatin and have no direct role in cell survival or cell cycle progression per se (Larson et al., 2019; Nagaraja et al., 2019; Silveira et al., 2019). Moreover, the mutant histones are essentially undruggable. Against this backdrop we undertook an unbiased genome wide CRISPR screen for DMG metabolic vulnerabilities. The dependencies identified in our screen included

previously documented reliance on cholesterol biosynthesis and TCA cycle dysregulation (Chung et al., 2020; Phillips et al., 2019). However, one remarkable and robust dependency identified is the *de novo* pyrimidine biosynthesis pathway. Deletion of any gene within this pathway led to cell lethality and the dependency was observed in all three DMG lines (Figure 1). The genetic phenotype is recapitulated by a potent (IC50 <1 nM) and specific DHODH inhibitor from Bayer (BAY2402234) that crosses the BBB, engages its target, and kills DMG cells *in vitro* and *in vivo* via induction of replication stress-mediated DNA damage (Figures 2,3, and 5). A companion manuscript (co-submitted) describes similar findings for IDH-mutant glioma--another aggressive glioma of young people which, like DMG, features an oncogenic driver that reconfigures tumor cell chromatin but has no intrinsic mitogenic function.

Purines and pyrimidines are the *sine qua non* of replicative DNA synthesis and the metabolic pathways involved in nucleotide biosynthesis have historically been attractive targets for cancer drug development. Indeed, one of the earliest chemotherapeutic agents, methotrexate, targets dihydrofolate reductase, a rate limiting enzyme within the folate metabolic pathway that is involved in nucleotide biosynthesis (Robinson et al., 2020). Accordingly, it is not surprising that multiple cancer cell types have shown themselves as vulnerable to inhibitors of *de novo* pyrimidine biosynthesis (Brown et al., 2017; Mathur et al., 2017; White et al., 2011). The list includes adult glioblastoma stem-like cells which are more sensitive to inhibition of *de novo* pyrimidine synthesis than their non-stem counterparts. However, unlike DMGs studied here that are selectively dependent on the *de novo* pyrimidine synthesis pathway, adult glioblastoma stem cells show a more predictable dependency on both the pyrimidine and purine *de novo* pathways (Wang et al., 2019b; Wang et al., 2017). The selective dependence of DMG cells on *de novo* pyrimidine synthesis but not purine synthesis is echoed by the IDH-mutant gliomas studied by Shi et al (co-submitted).

The selective response to suppression of the *de novo* pyrimidine biosynthesis pathway relative to the purine pathway documented in DMGs and IDH-mutant cancers is not entirely

understood. Recent studies highlight non-proliferative functions of *de novo* pyrimidine biosynthesis in cell differentiation (Siddiqui and Ceppi, 2020) and in mitochondrial function (Bennett et al., 2021; Mao et al., 2021). Developmental functions of the *de novo* pyrimidine biosynthesis pathway in DMG and IDH-mutant gliomas are especially plausible since both of these cancers are thought to arise from developmentally stalled progenitor cells that are locked into a replication competent state (Filbin et al., 2018; Pirozzi and Yan, 2021). Studies herein (Figures 3 and 5) and comparable studies by Shi et al. (co-submitted) show that replication stress, induced by DNA damage in DMG cells treated with BAY2402234, is sufficient to account for the therapeutic response.

Given the broad portfolio of proliferative and non-proliferative biological functions that require pyrimidines, the therapeutic window of a drug that blocks *de novo* pyrimidine biosynthesis would seem to be a concern. This concern is validated by the observation that targeted disruption of DHODH in mice causes embryonic lethality during organogenesis (http://www.informatics.jax.org). Notwithstanding the knockout phenotype, there are multiple reasons to expect a broad therapeutic window for DHODH antagonists. We note that DHODH and CAD are not included in the list of pan-cancer essential genes as defined by the DepMap, (the cancer dependency map at the Broad Institute). Indeed *CAD*, *DHODH* and *UMPS* are designated as “strongly selective” by DepMap which indicates that the dependency is not a common feature across ~1000 cell lines that have been screened using CRISPR-based gene knockout. Moreover, *in vivo* data from our studies and from Shi et al. (co-submitted) show that concentrations of BAY2402234 that inhibit DHODH in heart, liver and normal brain are well tolerated in mice. The discrepancy between embryonic lethality of DHODH knockout mice and non-essential status of the gene in somatic cells is not unprecedented. An early successful targeted therapeutic, imatinib, is well tolerated in adult patients with chronic myeloid leukemia (CML) and some patients have been treated with this drug for decades. However, several well-

established targets of imatinib, including Abl1, Abl2, and PDGFRA, are all lethal in murine knockout studies (Hoch and Soriano, 2003; Koleske et al., 1998; Soriano, 1997).

Drug resistance is an important concern and consideration in cancer medicine. If DMGs were treated with a DHODH antagonist as monotherapy, what would prevent selection of rare cells that can survive off the salvage pathway for pyrimidine biosynthesis or that express drug resistant variants of DHODH itself? Here, the synergistic response of DMGs to the combination of BAY2402234 and the ATR antagonist elimusertib suggests a strategy for suppression of drug resistance should the promise of BAY2402234 as monotherapy be realized. The serine/threonine protein kinase ATR regulates the intra-S-phase checkpoint and maintains genome stability in the presence of stalled replication forks that are induced by DHODH antagonists such as BAY2402234. Since, ATR plays no role in pyrimidine biosynthesis, drug resistance to combinatorial therapy for DMGs with drugs such as BAY2402234 and elimusertib would require the unlikely occurrence of concordant mutations in two independent biological pathways.

On a final note, it is worthy of mention that many oncogenic drivers and tumor suppressors that were first identified in childhood cancers, have gone on to prove widely relevant to adult cancers. Examples are replete: ETV6/RUNX1 (most common fusion in childhood acute lymphoblastic leukemia), EWSR1/FLI1 (gene fusion that defines Ewing sarcoma), and Wilms' tumor gene (WT1), to name only a few (Jiang et al., 2021; Rahal et al., 2018; Rosenfeld et al., 2003). Of relevance to this study and the work of Shi et al. (co-submitted), the histone H3 amino acid substitutions first observed in pediatric DMGs have now been reported in adult solid tumors such as acute myeloid leukemia, melanoma, and glioma (Lowe et al., 2019). Likewise, mutations in IDH1 or IDH2, first reported in gliomas of young adults, have since been noted as common driver mutations of acute myeloid leukemias that occur most commonly in older adults. For the road ahead, it will be of interest to see if DHODH

antagonists are efficacious in genetically informed clinical trials of these cancers, moving away from histology and toward genetic underpinnings to guide therapy.

ACKNOWLEDGEMENTS

We thank Dr. Charles D. Stiles, Dr. William G. Kaelin, Jr., and Dr. Samuel K. McBrayer for helpful suggestions and discussions, Dr. Myles Brown for providing the human CRISPR knockout libraries H1 and H3, Dr. Naiara Santana-Codina for help with cell-based metabolite analysis, and Dr. Shrabasti Roychowdhury for guidance in DNA fiber assays. This research was supported in part by the William M. Wood foundation (DHK). NYRA is supported by NIH grants U54-CA210180 (NYRA), P41-EB028741 (NYRA), T32EB025823 (SAS) and by the Pediatric Low-Grade Astrocytoma Program at PBTF (NYRA).

AUTHOR CONTRIBUTIONS

The work has been overseen and supervised by D.H.K. The conception and design of the work were driven by S.P, N.Y.R.A, D.C, and D.H.K. The execution of experiments, data collection and analysis were performed by S.P, J.P.K, H.N, S.A.S, M.S.R, L.A.M, M.G.F, and B.H. The manuscript has been assembled and written by S.P, S.A.S, K.X.L, M.G.F, N.Y.R.A, D.C, and D.H.K.

DECLARATION OF INTERESTS

Nathalie Y.R. Agar is key opinion leader for Bruker Daltonics, scientific advisor to Invicro, and receives support from Thermo Finnegan and EMD Serono. The other authors declare no competing interests.

FIGURE LEGENDS:

Figure 1. Genome-wide CRISPR screen identifies pathways critical for DMG cell survival

(A) Venn diagram shows the overlap of the genes identified as DMG dependencies in the three tested DMG cell lines.

(B) Ingenuity pathway analysis (IPA) defines DMG dependency pathways based on genes scored as dependency genes in at least two DMG cell lines.

(C) Schematic of the *de novo* and salvage pathways for pyrimidine synthesis (top). Volcano plots showing genes belonging to the Gene Ontology Resource (GO) pathway of pyrimidine biosynthesis (including uridine-5'-phosphate biosynthesis) whose depletion is significantly associated with DMG cell death (blue dots).

(D) Knockdown of *de novo* pyrimidine synthesis genes, *CAD* and *DHODH* using two distinct shRNAs inhibits DMG cell proliferation relative to control (scr) shRNA. Data is represented as mean±SEM (n=4).

See also Figures S1 and S2 and Tables S1, S2 and S3.

Figure 2. The DHODH inhibitor, BAY2402234, inhibits *de novo* pyrimidine synthesis and proliferation of DMGs

(A) DMG, adult GBM (aGBM), and normal human astrocytes (normal) were treated with increasing doses of BAY2402234 in quadruplicates for 5 days and IC50 was determined using PRISM software.

(B) Schematic representation of the metabolites in the *de novo* pyrimidine biosynthesis pathway and the enzymes catalyzing each reaction (blue; top). MALDI-mass spectroscopy analysis of soluble fraction of DMG cells treated with 1.25 nM BAY2402234 for 24 hours. The data show fold-change in metabolite peak intensity relative to control sample; p-values (ANOVA) are indicated for each metabolite. Data indicates mean±SEM (n=3).

See also Figures S3 and S4.

Figure 3. *De novo* pyrimidine biosynthesis inhibition by BAY2402234 inhibits DMG cell proliferation and induces DNA damage in DMG but not aGBM or normal astrocytes--all effects rescued by exogenous uridine supplementation

(A) Proliferation of DMG, normal human astrocytes, and aGBM cells treated with increasing doses of BAY2402234 and complete rescue of anti-proliferative effects with exogenous uridine (100 μM). Data is plotted as mean±SEM (n=4).

(B) Increased DNA damage, as measured by flow cytometry for γ-H2AX-positive cells, in BAY2402234-treated (1.25 nM; 48 hours) DMG cells with or without uridine supplementation (100 μM). aGBM line (BT954) shows no BAY2402234-induced increase in DNA damage. Data shows mean±SEM (n=3).

Figure 4. Mechanism of hyper-sensitivity of DMG cell to DHODH inhibition

(A-D) DMGs are not differentially sensitive to agents that broadly interfere with nucleotide synthesis and/or DNA replication. DMG and aGBM cells were treated with increasing doses of (A) *de novo* GMP synthesis inhibitor (VX-497), (B) 5-flourouracil (5-FU), (C) gemcitabine, and (D) hydroxyurea (HU) for 5 days in quadruplicates and IC50 values determined by PRISM software.

(E) mRNA expression of genes involved in pyrimidine homeostasis in DMG (red) and aGBM (blue) cell lines, quantified by RT-qPCR in triplicates and presented relative to normal astrocytes: *de novo* (left) and salvage (middle) pyrimidine synthesis and pyrimidine degradation (right).

(F) Inhibition of DPYD (gimeracil), an enzyme that catalyzes the first step of uracil degradation, partially rescues BAY2402234 sensitivity of DMG cells. Graphs shows mean±SEM (n=3).

Figure 5. DHODH inhibition arrests DMG cells in S phase, increases replication stress and induces apoptosis

(A) DMG cells treated with BAY2402234 (1.25 nM, 24 hours) were labeled with BrdU for 45 mins before cells were collected and analyzed by flow cytometry to measure S phase populations. Distribution of SU-DIPG4 cells (left panels) and quantification of S phase populations (right panel; mean±SEM ,n=3) in each DMG line after BAY2402234 treatment.

(B) BAY2402234-treated DMG cells [as in (A)] were analyzed for the presence of chromatin-bound RPA foci by immunofluorescence staining of RPA2. Hydroxyurea (HU), a known inducer of replication stress is included as a positive control. Uridine supplementation is used to document BAY2402234 on-target specificity for *de novo* pyrimidine synthesis. Violin plot shows the distribution of foci/cell in atleast 100 cells.

(C) Western blot analysis of whole cell extracts of SU-DIPG4 cells treated as in (B) to evaluate ATR signaling.

(D) DMG cells treated with BAY2402234 (1.25 nM, 48 hours; with or without 100µM uridine) were sequentially labeled with CldU and IdU to document replicating DNA using DNA combing assay. Fork speed was determined for at least 100 replicating fibers for each condition and represented as a violin plot. Representative image is shown on the left panel.

(E) DMG cells were treated as in (D) and apoptosis was quantified by cleaved CASPASE 3 (c-CASP3). Graph represents mean±SEM (n=3).

Figure 6. BAY2402234 is brain penetrant and inhibits *de novo* pyrimidine synthesis *in vivo* to prolong survival of mice bearing orthotopic DMG tumors

(A-C) MALDI MSI and optical microscopy imaging of brain tissue sections from mice harboring SU-DIPG13P* orthotopic tumor and treated with vehicle or BAY2402234 (4 mg/kg daily for 3 days). (A) Serial sagittal sections were stained with H&E and neighboring serial sections were

used for MALDI MSI to quantitate levels of BAY2402234 (left panel), and metabolites of *de novo* pyrimidine synthesis (right panel). Heme b was used as a marker of vasculature (left panel). BAY2402234 accumulated at 1.01 µM in the tumor region. Metabolites shown in right panel: N-carbamoyl-L-aspartate and dihydroorotate (upstream of DHODH), and UMP (downstream of DHODH). (B) Quantification of N-carbamoyl-L-aspartate, dihydroorotate, and UMP in brain sections from mice treated with BAY2402234 or vehicle (mean±SEM, n=3 per treatment) and analyzed by MALDI MSI, as in (A). (C) γ-H2AX staining of tumor regions in brain sections from vehicle- or BAY2402234-treated mice.

(D) Tumor growth monitored by weekly bioluminescence imaging (BLI) of mice with SU-DIPG13P* orthotopic tumor; data represent average BLI signal values±SEM.

(E) Quantification of immunohistochemical staining for Ki-67 in brain sections from vehicle- or BAY2402234-treated mice (mean±SEM, n=2 per treatment; SU-DIPG13P* orthotopic model).

(F) Kaplan-Meier curve delineating survival of mice bearing SU-DIPG13-P* orthotopic DMG tumors treated daily (until euthanasia) with vehicle or BAY2402234.

See also Figures S5 and S6.

Figure 7. ATR inhibition augments DHODH inhibitor-induced replication stress and DNA damage

(A) Quantification of RPA foci by immunostaining in DMG cells treated (24 hours) with BAY2402234 (1.25 nM), elimusertib (200 nM), or combination thereof. Data from atleast 100 cells is represented as a violin plot.

(B) Whole cell extracts of SU-DIPG4 cells treated as in (A) were immunoblotted with antibodies against indicated proteins.

See also Figure S7.

Figure 8. ATR- and DHODH-inhibition act synergistically to induce mitotic aberrations and cell death in DMG cells

(A) Flow cytometry quantitation of γ-H2AX-positive cells, in BAY2402234- (1.25 nM; 24 hours), ATR- (200 nM; 24 hours), or combination-treated SU-DIPG4 cultures, before (top panel) or 24 hours after (bottom panel) drug washout. Representative contour map shown in left panel; quantification (mean±SEM) shown in right panel.

(B) Metaphase spreads of SU-DIPG4 cells treated with BAY2402234 (1.25 nM; 24 hours), elimusertib (100 nM; 24 hours), or combination therapy and scored for mitotic abnormalities (i.e., chromatid/chromosomal breaks, radials, etc.). Left panel shows representative metaphase spread with red arrows indicating events scored as damage. Right panel shows quantification of at least 25 metaphase spreads scored per treatment.

(C) Synergistic cytotoxicity induced by combination therapy of DHODH- and ATR-inhibitors. DMG cells were treated with specified doses of BAY2402234 and elimusertib (72 hours; triplicates); cell viability was determined by Cell-Titer Glo and analyzed using Combenefit software to assess synergy-antagonism relationship.

MATERIALS AND METHODS

Drugs, cell culture, treatment, and drug sensitivity

The DHODH inhibitor, BAY2402234, and ATR inhibitor, elimusertib, were obtained from Bayer Inc. under a material transfer agreement. Hydroxyurea (HU) was purchased from Sigma-Aldrich, DPYD inhibitor, gimeracil, from MedChemExpress, and Vx-497, 5-fluorouracil (5-FU), and gemcitabine from Selleck Chemicals.

SF8628 was obtained from the Brain Tumor Research Center (BTRC) Tissue Bank at the University of California, San Francisco (UCSF, San Francisco, CA) and authenticated by the UCSF Genomics Core using short tandem repeat (STR) profiling. Cell lines BT145, BT189, BT333, BT424, BT954, BT924, BT189, BT869, SU-DIPG13, and SU-DIPG17 were obtained from The Center for Patient Derived Models (CPDM) at Dana-Farber Cancer Institute (DFCI); CCHMC-DIPG1 and CCHMC-DIPG2, referred as DIPG1 and DIPG2 were obtained from Dr. Rachid Drissi at Cincinnati Children's Hospital Medical Center. The SU-DIPG13P*, SU-DIPG4, SU-DIPG21, SU-DIPG33, and SU-DIPG36 lines were provided by Dr. Michelle Monje at Stanford University, and HSJD-DIPG007 was obtained from Dr. Angel Montero Carcaboso at Hospital Sant Joan de Deu, Barcelona, Spain. Immortalized astrocytes were purchased from ATCC. SF8628, and immortalized astrocytes were cultured as adherent cells in DMEM supplemented with 10% and 5% FBS, respectively. All other cell lines were cultured in 1:1 neurobasal media and DMEM F-12 with B27 supplement, 20 ng/mL EGF, 20 ng/mL FGF2, 10 ng/mL PDGF-AA, 10 ng/mL PDGF-BB, and 0.0002% heparin. For all cell-based assays, cells were plated in media supplemented with 10 nM uridine and for uridine rescue experiments, media was supplemented with 100 μM uridine. Unless specified, BAY2402234, elimusertib, and HU were used at a final concentration of 1.25 nM, 200 nM and 500 nM, respectively. To measure the sensitivity of DMG cells to various drugs as single agents or in combination

therapy, 500 cells were plated in quadruplicates in 96-well plates and treated as indicated. Cell viability was assessed by CellTiter-Glo assay after 3 or 5 days of drug treatment to determine the percentage of surviving cells and calculate IC50.

Genome wide screen for gene deletion using CRISPR

SF8628, DIPG1 and SU-DIPG13 ($2x10^8$ cells) were transduced with the human CRISPR sgRNA library by spinfection. For SF8628 and DIPG1 cells the H1 library (Addgene #1000000132) was used while the screen in SU-DIPG13 was performed using the H3 library (Addgene #133914). Cells were resuspended at $1x10^6$/ml in 50 ml tubes, mixed with pre-determined lentiviral supernatant volume that corresponds to a MOI (multiplicity of infection) of ~0.3 and 8 μg/ml polybrene (Santa Cruz Biotechnology) and centrifuged at 200 RPM for 45 minutes at room temperature. Cells were then resuspended and plated in 75 cm^2 flasks for 48 hours. After 48 hours, cells were collected and re-plated in fresh media with puromycin (SF8628 and SU-DIPG13: 2 μg/ml; DIPG1: 80 μg/ml). After 72 hours, half of the cells were collected by centrifugation, washed, and stored at -80^{o}C as the P0 sample. The remaining cells were collected, re-plated in fresh media and cultured for another 10 passages before they were harvested as P10 samples. At least 2-3$x10^7$ cells were plated at each passage. Two biological replicates of the screen were performed for each cell line.

To isolate genomic DNA, cell pellets were resuspended in DMS cell lysis buffer (10 mM Tris HCl pH 8.0, 1 mM EDTA, 0.2% SDS, 300 mM NaCl) at $1x10^7$ cells/ml with RNAase A at 100 mg/ml and incubated at 65^{o}C for 1 hour. Proteinase K was added at a final concentration of 100 mg/ml and incubated at 55^{o}C with rotation overnight. Next day, genomic DNA was purified by phenol:chloroform:isoamyl alcohol (25:24:1) extraction followed by isopropanol precipitation and 70% ethanol wash. The DNA was resuspended in water and re-extracted as above and finally dissolved in water and stored at 4^{o}C overnight before proceeding with library preparation. For library preparation, 200 mg of DNA per condition were PCR amplified using Q5 high fidelity

DNA polymerase (NEB Inc.) for 16 cycles using primers (Forward: 5'AATGGACTATCATATGCTTACCGTAACTTGAAAGTATTTCG3'; Reverse: 5'TCTACTATTCTTTCCCCTGCACTGTACCTGTGGGCGATGTGCGCTCTG3'). A second round of PCR was performed on the above amplified products for 8 cycles to attach Illumina sequencing adapters and to barcode samples. The PCR products were run on 2% agarose gel and purified using the gel purification kit before they were sent out for sequencing on the Illumina HiSeq (PE150) platform (Novagene Inc.).

MAGeCK was used to process and analyze the CRISPR screen data as follows (Li et al., 2014). First, for each sample, the count function of MAGeCK was used to map the paired-end sequencing data against the library to generate the sgRNA-level counts data for analysis. The mapping was performed separately for each of the two read sets against each of the two orientations of the library. The sgRNA-level counts dataset from the single read-library orientation combination with the highest mapping percentage was selected for further analysis. Quality control checks were performed based on the statistics generated from the MAGeCK's count function (Wang et al., 2019a). Most replicate samples had mapping success rates of at least 65%. There were two samples with mapping percentages lower than 65%, but above 60%. All day-0 samples had low Gini indices (<0.15), that are measures of evenness of sgRNA counts, and low percentages of zero-count sgRNAs (<1%). Next, the MAGeCK MLE was used to analyze the sgRNA-level counts data to determine whether the abundance of sgRNAs for each gene were different between P10 and P0 samples for each cell line. The analysis was performed on data of the two replicates together in paired mode and using the negative control sgRNAs that targeted the AAVS1 loci for normalization (Chen et al., 2018). We then determined the significant negatively selected genes from the MAGeCK MLE results of each cell line. A gene was considered as a significant negatively selected gene if it had a negative beta score and *p*-value of less than 0.01. To confirm the biological significance of these genes, we checked the representation of pan-cancer essential genes, and they represented a large fraction (>45%)

of the negatively selected genes. Finally we filtered out pan-cancer essential genes from the significant negatively selected genes to define the "DMG specific dependency genes" and performed pathway analysis on the gene set that was identified as DMG specific dependency in at least two of the DMG lines using the Core Analysis of IPA (QIAGEN Inc., https://www.qiagenbioinformatics.com/products/ingenuitypathway-analysis; release 2019-06-15).

Lentiviral production, infection of DMG cells, and proliferation assay

For lentiviral production, shRNA clones targeting *CAD* (TRCN0000045910, TRCN0000045908) and *DHODH* (TRCN0000025868, TRCN0000025839) were purchased from Sigma-Aldrich while a scrambled shRNA clone (Plasmid#1864) was bought from Addgene Inc. Briefly, 90% confluent HEK29T3 cells in 100 mm plates were transfected with pMD2.G (1.5 µg; Addgene plasmid # 12259), psPAX2 (3.0 µg; Addgene plasmid # 12260), and shRNA plasmid (6.6 µg) using Lipofectamine 2000 as per manufacturer's instructions. Viral supernatant was harvested at 48- and 72-hours post-transfection, combined, centrifuged at 3,000 rpm for 10 minutes to remove debris, and filtered through 0.45 µm filter. Viral supernatant was either immediately used or stored at −80°C. Five ml of the lentivirus containing supernatant was used to transduce $1x10^6$ DMG cells in the presence of 8 µg/mL polybrene and the cells were spun for 30 mins at 200 rpm before they were plated. After 16 hours, cells were harvested, 1000 cells were plated per well in fresh media in 96 well plates in quadruplicates, and the remaining cells were cultured for additional 48 hours before total RNA was extracted to measure gene knockdown using RT-qPCR. Cell proliferation was followed using CellTiter-Glo as per manufacturer's instruction in quadruplicates for each condition on Day 0, 3, 5 and 7 post-plating in 96 well plates and represented relative to day 0. To follow cell proliferation after BAY2402234 treatment, 500 cells per well were plated in quadruplicate in 96 well plates overnight before BAY2402234 was added and CellTiter-Glo signal was measured as above. To assess specificity of BAY2402234, cells

were plated and maintained in either low or high uridine media which included 10 nM or 100 µM supplementation of uridine, respectively.

Reverse transcriptase-quantitative polymerase chain reaction (RT-qPCR) assay

Total RNA was isolated for RT-PCR analysis using Trizol (Invitrogen). Reverse transcription was performed on 2 µg of total RNA using Superscript IV (Invitrogen Inc.) and real-time PCR was performed on Roche Light Cycler 96 using the specific primers with SYBR Green chemistry (see Table S4). Expression of mRNA was calculated using the $\Delta\Delta C_t$ method relative to scrambled shRNA-treated sample or to astrocytes and normalized to 18S rRNA.

Metabolite analysis on cultured cells

$2x10^6$ cells were plated overnight before addition of BAY2402234 for 24 hours. Next day, cells were supplemented with 2 ml of fresh media with or without drug and after 2 hours cells were harvested and processed in the cold room. Cells were collected by centrifugation and washed with cold saline solution. Pellets were resuspended in 300 mL of cold 80% methanol (LC-MS grade Honeywell catalog number 34966 diluted with LC-MS grade water from Pierce catalog number 51140) and incubated for 20 min at 4^{o}C in a shaker. Subsequently, samples were centrifuged to remove debris, 200 mL of the extract was transferred to a new tube, dried in a SpeedVac and stored at -80^{o}C until LC-MS analysis. For metabolite analysis samples were re-suspended in 20 mL HPLC grade water and 5-7 µL were injected and analyzed using a hybrid 6500 QTRAP triple quadrupole mass spectrometer (AB/SCIEX) coupled to a Prominence UFLC HPLC system (Shimadzu) via selected reaction monitoring (SRM) of a total of 289 endogenous water-soluble metabolites for steady-state analyses of samples as previously described (Yuan et al., 2012). Experiments were performed with three biological replicates and data were normalized using MinMax normalization across all measured metabolites in each sample before abundance of a metabolite was calculated relative to the DMSO treated sample.

Cell cycle, apoptosis, and γ-H2AX detection assays

To determine cell cycle profiles, $1x10^5$ cells were plated in 2 ml media overnight and treated with 1.25 nM BAY2402234 for 24 hours before cells were harvested and fixed in 70% ethanol at -20°C overnight. Cells were washed with 1X PBS and stained with propidium iodide solution containing RNaseA (Cell Signaling Technology). Data were collected by flow cytometry (CytoflexS) and analyzed using ModFit *LT* software. To precisely quantify S-phase cell population, $1x10^5$ cells were plated in 2 ml media overnight and treated with 1.25 nmol/L BAY2402234 for 24 hours before cells were incubated in the presence of BrdU for 45 mins and harvested for analysis of BrdU positive cells using the BrdU flow kit according to manufacturer's protocol (BD Biosciences). Data were collected on CytoflexS and analyzed by FlowJo software.

To detect and measure apoptotic cell populations, cleaved CASPASE3 was measured by flow cytometry and analyzed by FlowJo software. 1×10^5 cells were treated with 1.25 nM BAY2402234 for 48 hours before cells were harvested and fixed in 4% paraformaldehyde for 15 minutes. Cells were then permeabilized and re-fixed in cold 90% methanol overnight. Cells were washed on the following day, blocked in 1X PBS containing 1 mg/ml BSA and 2.5 µl of human FcX-TruStain (Biolegend Inc.) for 15 minutes and incubated with PE-c-CASPASE3 antibody (Cell Signaling #9978) for 1 hour before cells were washed and data collected on CytoflexS. To detect DNA damage, γ-H2AX-positive cells were determined after 24 hours of exposure to 1.25 nM BAY2402234 using flow cytometry as described previously (Pal et al., 2018).

Western blotting, immunofluorescence, DNA fiber assay, and metaphase spreads

$10x10^6$ cells were treated with DMSO, BAY2402234, elimusertib, or HU for 24 hours before whole cell lysates were prepared in UTB buffer (50 mM Tris-HCl pH 7.5, 8M Urea, 150 mM β-mercaptoethanol) supplemented with complete mini protease inhibitor cocktail (Roche) and

phosphatase inhibitor cocktail (Roche) and sonicated. Whole cell lysate (25-60 mg) was separated by SDS-PAGE, transferred to PDVF membrane, blocked, and incubated with primary antibody at recommended dilution overnight before secondary antibody incubation and detection with ECL reagent. Primary antibodies used are anti- RPA2 (ab2175, Abcam Inc.), phospho-RPA2-T21 (ab61065, Abcam Inc.), phospho-RPA2S32/33 (A300-246A, Bethyl laboratories), γ-H2AX (05-636, Millipore), phospho-CHK1S345 (#2348, Cell Signaling Technologies), cleaved PARP1 (#5625, Cell Signaling Technologies), and β-ACTIN (#3700, Cell Signaling Technologies).

For detection of chromatin-bound RPA by immunofluorescence staining, cells were plated overnight, then treated with BAY2402234, elimusertib, HU, or DMSO for 24 hours. Cells were harvested and pre-extracted in 1X PBS containing 0.5% Triton-X100 on ice for 10 min before being washed and fixed in 4% paraformaldehyde for 15 minutes. Cells were blocked in 1X PBS containing 3% goat serum, 0.1% Triton X-100, 1 mmol/L EDTA, and 1 mg/mL BSA for 1 hour and cytospun onto super-frosted slides. Slides were dried for 10 minutes and then incubated with primary antibody (RPA2 at 1:200, ab2175, Abcam Inc.; γ-H2AX at 1:1000, 05-636, Millipore) in blocking buffer overnight at 4°C. After overnight incubations, slides were washed prior to incubation with fluorophore conjugated secondary antibody solution for 1 hour. Slides were washed, nuclei counterstained with DAPI and mounted. Images were taken at 63X magnification using the Zeiss microscope and number of RPA foci and γ-H2AX staining intensity per nucleus were determined using CellProfiler software for at least 100 cells per condition.

To study impacts on replication fork progression, replicating DNA was labeled and analyzed by DNA fiber assays. Briefly, after 24 hours of DMSO or BAY2402234 treatment, cells were pulsed with 50 mM of CldU (Sigma-Aldrich, C-6891) for 20 minutes, washed and again pulsed with 250 mM of IdU (Sigma-Aldrich, I-7125) for 20 minutes followed by washing and accutase treatment to get single cell suspensions. Next, $2x10^4$ cells were embedded in agarose

plugs and processed using the FiberPrepKit (Genomic Vision, EXT-001) according to manufacturer's instructions. The plugs were treated with protease overnight at 50^{o}C, washed extensively, agarose was melted and digested overnight with β-agarose at 42^{o}C before DNA solutions were combed on coated coverslips (Genomic Vision) using the FiberComb Molecular Coming System; coverslips were dehydrated for 2 hours at 60^{o}C and stored at -20^{o}C until immunodetection. Next, coverslips were subjected to chemical denaturation in fresh solution containing 0.5M NaOH and 1M NaCl for 8 minutes at room temperature, washed and dehydrated sequentially in 70%, 90%, and 100% ethanol bath for 3 minutes each. Immunodetection of the replication tracks was performed using primary antibodies diluted in 1% BSA [Rat anti-CldU (Abcam, ab6326); mouse anti-IdU (BD Biosciences, 347580)] for 110 minutes at 37^{o}C followed by washing and secondary antibodies goat anti-rat Cy5 (Abcam, ab6565) and goat anti-mouse Cy3.5 (Abcam, ab6946) for 45 minutes at 37^{o}C. To visualize single stranded DNA (ssDNA), coverslips were also stained with mouse anti-ssDNA (DSHB University of Iowa) for 75 minutes at 37^{o}C and detected with goat anti-mouse BV480 (BD Biosciences, 564877) for 45 minutes at 37^{o}C. During immunodetection all washes were performed with 1X PBS containing 0.05% Tween-20 for 3 minutes and repeated x3. Finally, coverslips were dehydrated in 70%, 90%, and 100% ethanol bath for 3 minutes each, dried, mounted on slides (Genomic Vision) and scanned using the Fiber Vision automated scanner (Genomic Vision). Image analysis and fiber measurements were done using ImageJ software. The red and green signals were measured, and fork speeds were calculated.

Cell cultures treated with DHODHi and/or ATRi for 24 hours were harvested and washed twice in 20-fold excess media to remove drugs before re-plating in drug-free fresh media. After 3-4 hours, 30 ng/mL of Colcemid (Roche) was added and cultures were incubated for an additional 17 hours to arrest cells at metaphase. Cells were harvested and treated with accutase to obtain single cell suspension. Next, cells were collected by centrifugation and treated with warm hypotonic solution (0.075M KCl) for 20 minutes at 37^{o}C. Following hypotonic

treatment, fresh fixative (3-parts methanol:1-part acetic acid) was added to the cells for 10 minutes at room temperature. The fixing step was repeated three times. To make slides, cells were resuspended in a fresh fixative solution of methanol and acetic acid, dropped on a pre-cleaned slide, and stained with Giemsa stain. Analysis was performed on a brightfield microscope at 100X magnification. Mitotic abnormalities were visually scored and at least 25 metaphase spreads were scored for each condition.

Establishment of orthotopic tumor in mice

All animal studies were performed according to Dana-Farber Cancer Institute Institutional Animal Care and Use Committee (IACUC)-approved protocols. Animals were injected intraperitoneally with the analgesic buprenorphine 0.05 mg/kg and then anesthetized with isoflurane 2–3% mixed with medical air and placed on a stereotactic frame. Next, a small incision and a hole was made with a 25-gauge needle and SU-DIPG13-P* or DIPG1 cells expressing luciferase gene ($1x10^5$ cells for SU-DIPG13P* or $5x10^4$ cells for DIPG1; in 3 µl PBS) were injected stereo-tactically into the right pons (stereotactic coordinates zeroed on bregma: -1.5 mm X(ML), -5.5 mm Y(AP) and -5.0 mm Z(DV)) of 5 weeks-old female NSG mice (NOD.Cg-Prkdcscid Il2rgtm1Wjl/SzJ, The Jackson Laboratory, Bar Harbor, ME) at rate of 1 µl/min with use of an infusion pump before the incision was closed. Mice were then checked daily for signs of distress, including seizures, weight loss, or tremors, and euthanized as they developed neurological symptoms, including head tilt, seizures, sudden weight loss, loss of balance, and/or ataxia.

Bioluminescence imaging and *in vivo* treatment

Tumor growth was monitored weekly using the IVIS Spectrum In Vivo Imaging System (PerkinElmer), starting at day 8 post-cell injections. Briefly, mice were injected subcutaneously with 75 mg/kg D-luciferin potassium salt (Promega E1605) in sterile PBS and anesthetized with

2% isoflurane in medical air. Serial bioluminescence images were acquired using automated exposure set-up. Peak bioluminescence signal intensity within selected regions of interest was quantified using the Living Image Software (PerkinElmer) and expressed as photon flux (ph/sec/cm^2/sr). Mice were treated orally with BAY2402234 (4 mg/Kg) or vehicle once daily until euthanasia for efficacy studies and for 4 consecutive days for the pharmacodynamic study before mice were euthanized and brain tissues were harvested. BAY2402234 was formulated in 90% PEG400 and 10% ethanol and administered by oral gavage.

Tumor and tissue analysis by MALDI mass spectroscopy and microscopy

Tissue preparation for MALDI MSI and microscopy: Mouse brains were dissected, snap-frozen in liquid nitrogen, and stored at -80^{0}C. Sagittal cryosections of 10 µm thickness were collected from each mouse brain and thaw-mounted onto indium tin oxide (ITO) slides. Whole healthy mouse control brain tissues were homogenized and spiked with BAY2402234 concentrations ranging from 0.2-50 µM. The nine spiked homogenates were then dispensed into a nine-well gelatin (40%) tissue microarray array (TMA) mold with 1.5 mm core diameter channels to create a quantitative tissue mimetics array. The tissue mimetics were frozen and cryo-sectioned at the same thickness as the mouse brain tissues and underwent the same sample preparation. Serial sections were obtained for MALDI MSI, hematoxylin and eosin (H&E), γ-H2AX immunostaining and DAPI staining. Optical and fluorescence microscopy images were acquired using 10X and 40X objectives (Zeiss Observer Z.1, Oberkochen, Germany) and a FITC filter.

MALDI Matrix preparation and application: For BAY2402234 tissue quantification, a 2,5-dihydroxybenzoic acid (160 mg/mL) matrix solution dissolved in 70:30 methanol: 0.1% TFA with 1% DMSO was used. The matrix was applied onto tissue sections using a TM sprayer (HTX Technologies, Chapel Hill, NC) with a two-pass cycle at a flow rate (0.18 mL/min), spray nozzle velocity (1200 mm/min), nitrogen gas pressure (10 psi), spray nozzle temperature (75°C), and track spacing (2 mm). A recrystallization step was performed with 5% acetic acid solution at

85°C for 6 minutes. Dihydroorotate, N-carbamoyl-L-aspartate, and uridine monophosphate (UMP) were imaged using a 1,5-diaminonaphthalene hydrochloride (4.3 mg/mL) matrix solution in 4.5/5/0.5 HPLC grade water/ethanol/1 M HCl (v/v/v). The TM-sprayer parameters included a four-pass cycle with a flow rate (0.09 mL/min), spray nozzle velocity (1200 mm/min), spray nozzle temperature (75°C), nitrogen gas pressure (10 psi), track spacing (2 mm).

MALDI MRM mass spectrometry imaging: Tissue and tissue mimetic sections were imaged using a timsTOF fleX mass spectrometer (Bruker Daltonics, Billerica, MA) operating in positive ion mode by multiple reaction monitoring (MRM) scanning between *m/z* 100-650. A BAY2402234 solution was infused through the ESI source to optimize the MRM settings, ion transfer funnels, quadrupole, collision cell, and focus pre-TOF parameters. The optimal collision energy for the BAY2402234 precursor was 35 eV with a 3 *m/z* isolation width for the precursor to product ion transition 521.101→376.091 corresponding to $[C_{21}H_{18}ClF_5N_4O_4+H]^+$ and $[C_{15}H_{12}F_4N_3O_4+H]^+$, respectively (SI Fig 1. a). The ESI method was then transferred to a MALDI source method and tuned using an Agilent tune mix solution (Agilent Technologies, Santa Clara, CA). For the MALDI MSI conditions, the laser repetition rate was set to 10,000 Hz, with 2,000 laser shots per 50 µm pixel size. Data visualization using SCiLS Lab software (version 2021a premium, Bruker Daltonics, Billerica, MA) was used without data normalization. A linear regression correlating the ion intensity and BAY2402234 concentration range between 0.2-2 µM from the tissue mimetic was established with a correlation coefficient of 0.994 (SI Fig 1. bc). Limit of detection (LOD) of 0.11 µM (S/N ratio of >3) and limit of quantification (LOQ) of 0.35 µM (S/N ratio of >10) were calculated.

Metabolite MALDI MSI: Dihydroorotate, N-carbamoyl-L-aspartate, and UMP were imaged from the BAY2402234 dosed and vehicle tissue sections with the Q-TOF instrument operated in negative ion mode in full scan mode for *m/z* 50-400. Standard solutions were infused using the ESI source to optimize the instrument parameters. Dihydroorotate and N-

carbamoyl-L-aspartate fragmented in full MS scan mode, so their product ions were directly monitored in MS mode by setting the collision energy to 10 eV. The product ion monitored for dihydroorotate was *m/z* 113.037 $[C_4H_6N_2O_2\text{-}H]^-$ and for N-carbamoyl-L-aspartate *m/z* 132.031 $[C_4H_7NO_4\text{-}H]^-$ (SI Fig 2. b). Using a serial section, a full scan approach was used to image UMP by monitoring its precursor ion at *m/z* 323.029 $[C_9H_{13}N_2O_9P\text{-}H]^-$. All metabolites were confirmed using direct on-tissue MSMS and compared to standards under the same analytical conditions.

Statistical analysis

Unless indicated, all data are represented as mean ± SEM and plotted using PRISM software. IC_{50} for drug responses were calculated using the PRISM software. For two group comparisons, the t-test was used. Whenever multiple groups were compared, one-way ANOVA was used, and Tukey test was performed to correct for multiple comparisons in PRISM. For datasets that failed normality test, we performed nonparametric Kruskal-Wallis testing with Dunn's test to correct for multiple comparisons in PRISM. Asterisks indicate statistically significant (*, $P<0.05$; **, $P<10^{-2}$; ***, $P<10^{-3}$; ****, $P<10^{-4}$) values.

SUPPLEMENTAL INFORMATION

Supplemental Figure 1 (Related to Figure 1): Flow chart of CRISPR screen workflow in DMG cell lines.

Supplemental Figure 2 (Related to Figure 1): shRNA knockdown of *CAD* and *DHODH* expression in DMG cells.

Supplemental Figure 3 (Related to Figure 2): Lack of correlation between cell proliferation and BAY2402234 sensitivity.

Supplemental Figure 4 (Related to Figure 2): DHODH inhibition severely depletes UMP in DMG but not aGBM.

Supplemental Figure 5 (Related to Figure 6): MALDI-MSI analysis of brain sections from mice treated with BAY2402234 or vehicle.

Supplemental Figure 6 (Related to Figure 6): BAY2402234 treatment hinders tumor growth and improves overall survival in a highly aggressive DMG orthotropic model, DIPG1.

Supplemental Figure 7 (Related to Figure 7): Combination of ATR- and DHODH-inhibition augments DNA damage but does not affect the $pRPA^{T21}$ phosphorylation that is induced by replication stress in an ATR-independent fashion.

Supplemental Table 1 (Related to Figure 1). Gene list defined as common essential genes based on DepMap

Supplemental Table 2 (Related to Figure 1). Representation of pan-cancer essential genes among the top negatively selected genes required for cell viability.

Supplemental Table 3 (Related to Figure 1). DMG dependency genes identified in each DMG line using CRISPR screen

Supplemental Table 4 (Related to Figures 4 and S2). Sequence of primers used for quantitative polymerase chain reaction (PCR) assays.

REFERENCES

Bender, S., Tang, Y., Lindroth, A. M., Hovestadt, V., Jones, D. T., Kool, M., Zapatka, M., Northcott, P. A., Sturm, D., Wang, W., *et al.* (2013). Reduced H3K27me3 and DNA hypomethylation are major drivers of gene expression in K27M mutant pediatric high-grade gliomas. Cancer Cell *24*, 660-672.

Bennett, C. F., O'Malley, K. E., Perry, E. A., Balsa, E., Latorre-Muro, P., Riley, C. L., Luo, C., Jedrychowski, M., Gygi, S. P., and Puigserver, P. (2021). Peroxisomal-derived ether phospholipids link nucleotides to respirasome assembly. Nat Chem Biol *17*, 703-710.

Braunstein, S., Raleigh, D., Bindra, R., Mueller, S., and Haas-Kogan, D. (2017). Pediatric high-grade glioma: current molecular landscape and therapeutic approaches. J Neurooncol *134*, 541-549.

Brown, K. K., Spinelli, J. B., Asara, J. M., and Toker, A. (2017). Adaptive Reprogramming of De Novo Pyrimidine Synthesis Is a Metabolic Vulnerability in Triple-Negative Breast Cancer. Cancer Discov *7*, 391-399.

Buczkowicz, P., Hoeman, C., Rakopoulos, P., Pajovic, S., Letourneau, L., Dzamba, M., Morrison, A., Lewis, P., Bouffet, E., Bartels, U., *et al.* (2014). Genomic analysis of diffuse intrinsic pontine gliomas identifies three molecular subgroups and recurrent activating ACVR1 mutations. Nat Genet *46*, 451-456.

Castel, D., Kergrohen, T., Tauziede-Espariat, A., Mackay, A., Ghermaoui, S., Lechapt, E., Pfister, S. M., Kramm, C. M., Boddaert, N., Blauwblomme, T., *et al.* (2020). Histone H3 wild-type DIPG/DMG overexpressing EZHIP extend the spectrum diffuse midline gliomas with PRC2 inhibition beyond H3-K27M mutation. Acta Neuropathol *139*, 1109-1113.

Chen, C. H., Xiao, T., Xu, H., Jiang, P., Meyer, C. A., Li, W., Brown, M., and Liu, X. S. (2018). Improved design and analysis of CRISPR knockout screens. Bioinformatics *34*, 4095-4101.

Chung, C., Sweha, S. R., Pratt, D., Tamrazi, B., Panwalkar, P., Banda, A., Bayliss, J., Hawes, D., Yang, F., Lee, H. J., *et al.* (2020). Integrated Metabolic and Epigenomic Reprograming by H3K27M Mutations in Diffuse Intrinsic Pontine Gliomas. Cancer Cell *38*, 334-349 e339.

Cooney, T., Lane, A., Bartels, U., Bouffet, E., Goldman, S., Leary, S. E. S., Foreman, N. K., Packer, R. J., Broniscer, A., Minturn, J. E., *et al.* (2017). Contemporary survival endpoints: an International Diffuse Intrinsic Pontine Glioma Registry study. Neuro Oncol *19*, 1279-1280.

Filbin, M. G., Tirosh, I., Hovestadt, V., Shaw, M. L., Escalante, L. E., Mathewson, N. D., Neftel, C., Frank, N., Pelton, K., Hebert, C. M., *et al.* (2018). Developmental and oncogenic programs in H3K27M gliomas dissected by single-cell RNA-seq. Science *360*, 331-335.

Harutyunyan, A. S., Krug, B., Chen, H., Papillon-Cavanagh, S., Zeinieh, M., De Jay, N., Deshmukh, S., Chen, C. C. L., Belle, J., Mikael, L. G., *et al.* (2019). H3K27M induces defective chromatin spread of PRC2-mediated repressive H3K27me2/me3 and is essential for glioma tumorigenesis. Nat Commun *10*, 1262.

Hoch, R. V., and Soriano, P. (2003). Roles of PDGF in animal development. Development *130*, 4769-4784.

Jiang, T., Wang, G., Liu, Y., Feng, L., Wang, M., Liu, J., Chen, Y., and Ouyang, L. (2021). Development of small-molecule tropomyosin receptor kinase (TRK) inhibitors for NTRK fusion cancers. Acta Pharm Sin B *11*, 355-372.

Jones, C., Karajannis, M. A., Jones, D. T. W., Kieran, M. W., Monje, M., Baker, S. J., Becher, O. J., Cho, Y. J., Gupta, N., Hawkins, C., *et al.* (2017). Pediatric high-grade glioma: biologically and clinically in need of new thinking. Neuro Oncol *19*, 153-161.

Khuong-Quang, D. A., Buczkowicz, P., Rakopoulos, P., Liu, X. Y., Fontebasso, A. M., Bouffet, E., Bartels, U., Albrecht, S., Schwartzentruber, J., Letourneau, L., *et al.* (2012). K27M mutation in histone H3.3 defines clinically and biologically distinct subgroups of pediatric diffuse intrinsic pontine gliomas. Acta Neuropathol *124*, 439-447.

Koleske, A. J., Gifford, A. M., Scott, M. L., Nee, M., Bronson, R. T., Miczek, K. A., and Baltimore, D. (1998). Essential roles for the Abl and Arg tyrosine kinases in neurulation. Neuron *21*, 1259-1272.

Krug, B., De Jay, N., Harutyunyan, A. S., Deshmukh, S., Marchione, D. M., Guilhamon, P., Bertrand, K. C., Mikael, L. G., McConechy, M. K., Chen, C. C. L., *et al.* (2019). Pervasive H3K27 Acetylation Leads to ERV Expression and a Therapeutic Vulnerability in H3K27M Gliomas. Cancer Cell *35*, 782-797 e788.

Larson, J. D., Kasper, L. H., Paugh, B. S., Jin, H., Wu, G., Kwon, C. H., Fan, Y., Shaw, T. I., Silveira, A. B., Qu, C., *et al.* (2019). Histone H3.3 K27M Accelerates Spontaneous Brainstem Glioma and Drives Restricted Changes in Bivalent Gene Expression. Cancer Cell *35*, 140-155 e147.

Li, W., Xu, H., Xiao, T., Cong, L., Love, M. I., Zhang, F., Irizarry, R. A., Liu, J. S., Brown, M., and Liu, X. S. (2014). MAGeCK enables robust identification of essential genes from genome-scale CRISPR/Cas9 knockout screens. Genome Biol *15*, 554.

Lowe, B. R., Maxham, L. A., Hamey, J. J., Wilkins, M. R., and Partridge, J. F. (2019). Histone H3 Mutations: An Updated View of Their Role in Chromatin Deregulation and Cancer. Cancers (Basel) *11*.

Luo, J., Solimini, N. L., and Elledge, S. J. (2009). Principles of cancer therapy: oncogene and non-oncogene addiction. Cell *136*, 823-837.

Mackay, A., Burford, A., Carvalho, D., Izquierdo, E., Fazal-Salom, J., Taylor, K. R., Bjerke, L., Clarke, M., Vinci, M., Nandhabalan, M., *et al.* (2017). Integrated Molecular Meta-Analysis of 1,000 Pediatric High-Grade and Diffuse Intrinsic Pontine Glioma. Cancer Cell *32*, 520-537 e525.

Mao, C., Liu, X., Zhang, Y., Lei, G., Yan, Y., Lee, H., Koppula, P., Wu, S., Zhuang, L., Fang, B., *et al.* (2021). DHODH-mediated ferroptosis defence is a targetable vulnerability in cancer. Nature *593*, 586-590.

Mathur, D., Stratikopoulos, E., Ozturk, S., Steinbach, N., Pegno, S., Schoenfeld, S., Yong, R., Murty, V. V., Asara, J. M., Cantley, L. C., and Parsons, R. (2017). PTEN Regulates Glutamine Flux to Pyrimidine Synthesis and Sensitivity to Dihydroorotate Dehydrogenase Inhibition. Cancer Discov *7*, 380-390.

Nagaraja, S., Quezada, M. A., Gillespie, S. M., Arzt, M., Lennon, J. J., Woo, P. J., Hovestadt, V., Kambhampati, M., Filbin, M. G., Suva, M. L., *et al.* (2019). Histone Variant and Cell Context

Determine H3K27M Reprogramming of the Enhancer Landscape and Oncogenic State. Mol Cell *76*, 965-980 e912.

Nagaraja, S., Vitanza, N. A., Woo, P. J., Taylor, K. R., Liu, F., Zhang, L., Li, M., Meng, W., Ponnuswami, A., Sun, W., *et al.* (2017). Transcriptional Dependencies in Diffuse Intrinsic Pontine Glioma. Cancer Cell *31*, 635-652 e636.

Ostrom, Q. T., Gittleman, H., Liao, P., Vecchione-Koval, T., Wolinsky, Y., Kruchko, C., and Barnholtz-Sloan, J. S. (2017). CBTRUS Statistical Report: Primary brain and other central nervous system tumors diagnosed in the United States in 2010-2014. Neuro Oncol *19*, v1-v88.

Pagliarini, R., Shao, W., and Sellers, W. R. (2015). Oncogene addiction: pathways of therapeutic response, resistance, and road maps toward a cure. EMBO Rep *16*, 280-296.

Pal, S., Kozono, D., Yang, X., Fendler, W., Fitts, W., Ni, J., Alberta, J. A., Zhao, J., Liu, K. X., Bian, J., *et al.* (2018). Dual HDAC and PI3K Inhibition Abrogates NFkappaB- and FOXM1-Mediated DNA Damage Response to Radiosensitize Pediatric High-Grade Gliomas. Cancer Res *78*, 4007-4021.

Phillips, R. E., Yang, Y., Smith, R. C., Thompson, B. M., Yamasaki, T., Soto-Feliciano, Y. M., Funato, K., Liang, Y., Garcia-Bermudez, J., Wang, X., *et al.* (2019). Target identification reveals lanosterol synthase as a vulnerability in glioma. Proc Natl Acad Sci U S A *116*, 7957-7962.

Pirozzi, C. J., and Yan, H. (2021). The implications of IDH mutations for cancer development and therapy. Nat Rev Clin Oncol *18*, 645-661.

Rahal, Z., Abdulhai, F., Kadara, H., and Saab, R. (2018). Genomics of adult and pediatric solid tumors. Am J Cancer Res *8*, 1356-1386.

Robinson, A. D., Eich, M. L., and Varambally, S. (2020). Dysregulation of de novo nucleotide biosynthetic pathway enzymes in cancer and targeting opportunities. Cancer Lett *470*, 134-140.

Rosenfeld, C., Cheever, M. A., and Gaiger, A. (2003). WT1 in acute leukemia, chronic myelogenous leukemia and myelodysplastic syndrome: therapeutic potential of WT1 targeted therapies. Leukemia *17*, 1301-1312.

Saldivar, J. C., Cortez, D., and Cimprich, K. A. (2017). The essential kinase ATR: ensuring faithful duplication of a challenging genome. Nat Rev Mol Cell Biol *18*, 622-636.

Siddiqui, A., and Ceppi, P. (2020). A non-proliferative role of pyrimidine metabolism in cancer. Mol Metab *35*, 100962.

Silveira, A. B., Kasper, L. H., Fan, Y., Jin, H., Wu, G., Shaw, T. I., Zhu, X., Larson, J. D., Easton, J., Shao, Y., *et al.* (2019). H3.3 K27M depletion increases differentiation and extends latency of diffuse intrinsic pontine glioma growth in vivo. Acta Neuropathol *137*, 637-655.

Soriano, P. (1997). The PDGF alpha receptor is required for neural crest cell development and for normal patterning of the somites. Development *124*, 2691-2700.

Sturm, D., Pfister, S. M., and Jones, D. T. W. (2017). Pediatric Gliomas: Current Concepts on Diagnosis, Biology, and Clinical Management. J Clin Oncol *35*, 2370-2377.

Wang, B., Wang, M., Zhang, W., Xiao, T., Chen, C. H., Wu, A., Wu, F., Traugh, N., Wang, X., Li, Z., *et al.* (2019a). Integrative analysis of pooled CRISPR genetic screens using MAGeCKFlute. Nat Protoc *14*, 756-780.

Wang, X., Yang, K., Wu, Q., Kim, L. J. Y., Morton, A. R., Gimple, R. C., Prager, B. C., Shi, Y., Zhou, W., Bhargava, S., *et al.* (2019b). Targeting pyrimidine synthesis accentuates molecular therapy response in glioblastoma stem cells. Sci Transl Med *11*.

Wang, X., Yang, K., Xie, Q., Wu, Q., Mack, S. C., Shi, Y., Kim, L. J. Y., Prager, B. C., Flavahan, W. A., Liu, X., *et al.* (2017). Purine synthesis promotes maintenance of brain tumor initiating cells in glioma. Nat Neurosci *20*, 661-673.

White, R. M., Cech, J., Ratanasirintrawoot, S., Lin, C. Y., Rahl, P. B., Burke, C. J., Langdon, E., Tomlinson, M. L., Mosher, J., Kaufman, C., *et al.* (2011). DHODH modulates transcriptional elongation in the neural crest and melanoma. Nature *471*, 518-522.

Wu, G., Broniscer, A., McEachron, T. A., Lu, C., Paugh, B. S., Becksfort, J., Qu, C., Ding, L., Huether, R., Parker, M., *et al.* (2012). Somatic histone H3 alterations in pediatric diffuse intrinsic pontine gliomas and non-brainstem glioblastomas. Nat Genet *44*, 251-253.

Yuan, M., Breitkopf, S. B., Yang, X., and Asara, J. M. (2012). A positive/negative ion-switching, targeted mass spectrometry-based metabolomics platform for bodily fluids, cells, and fresh and fixed tissue. Nat Protoc *7*, 872-881.

Figure 1

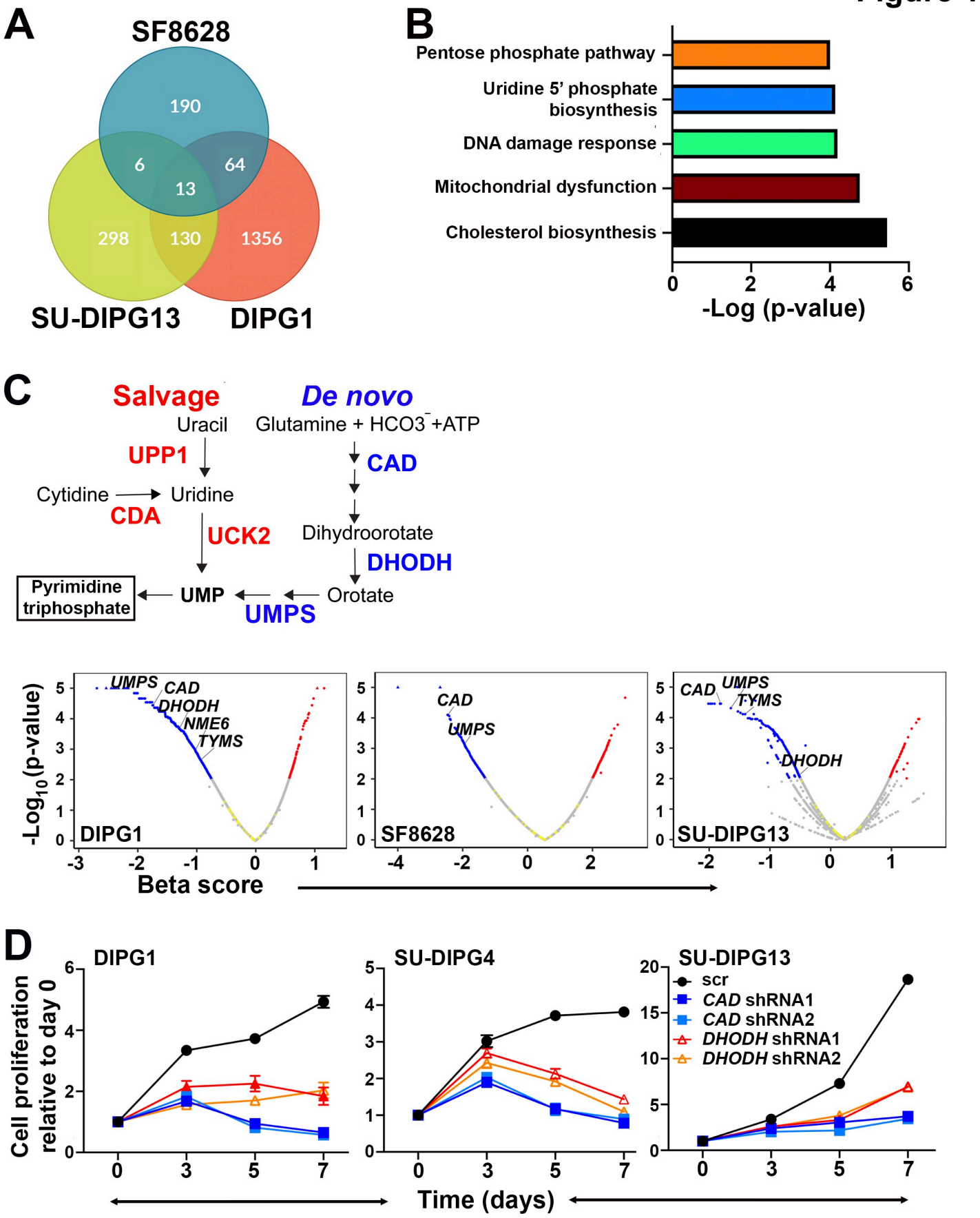

Figure 2

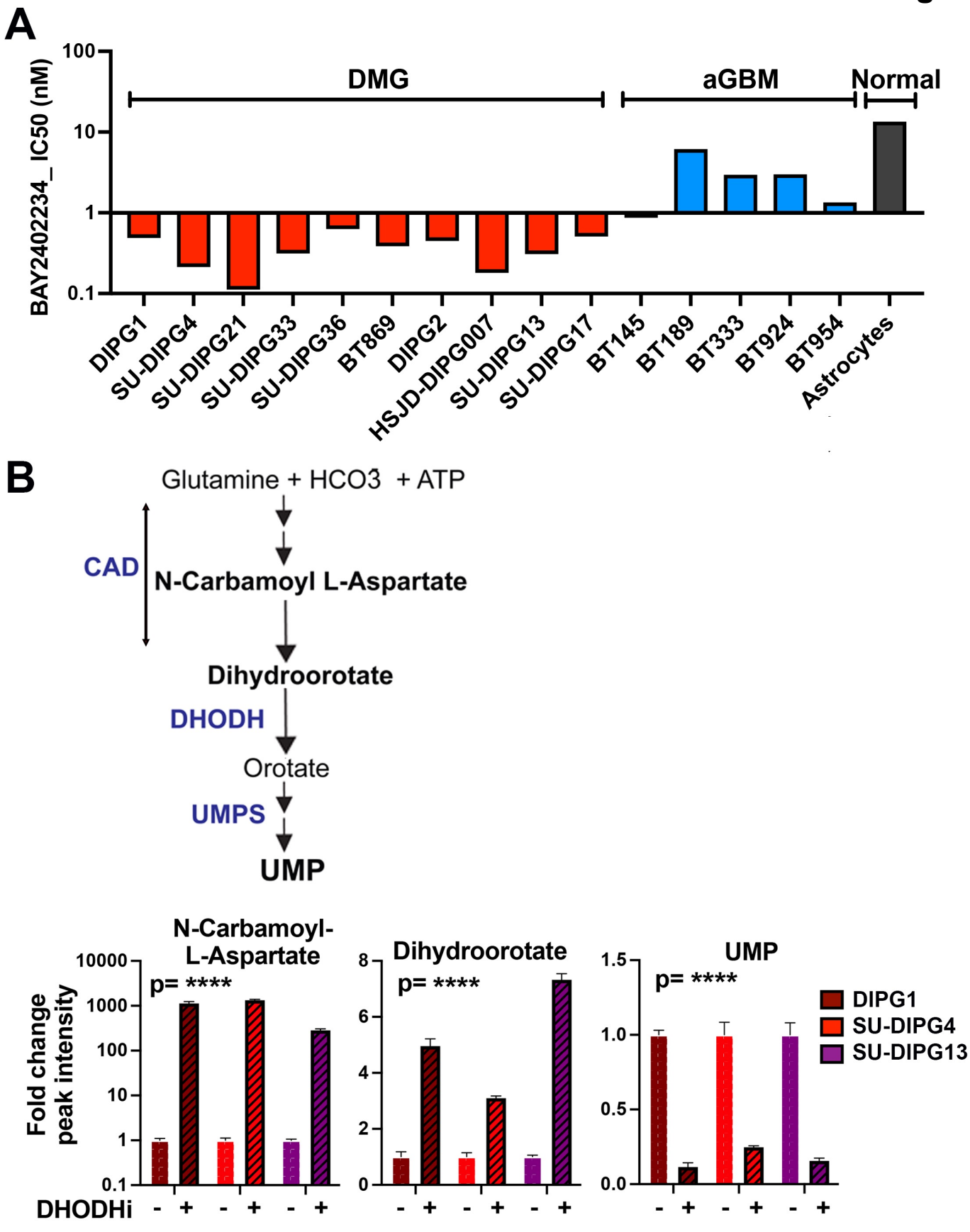

Figure 3

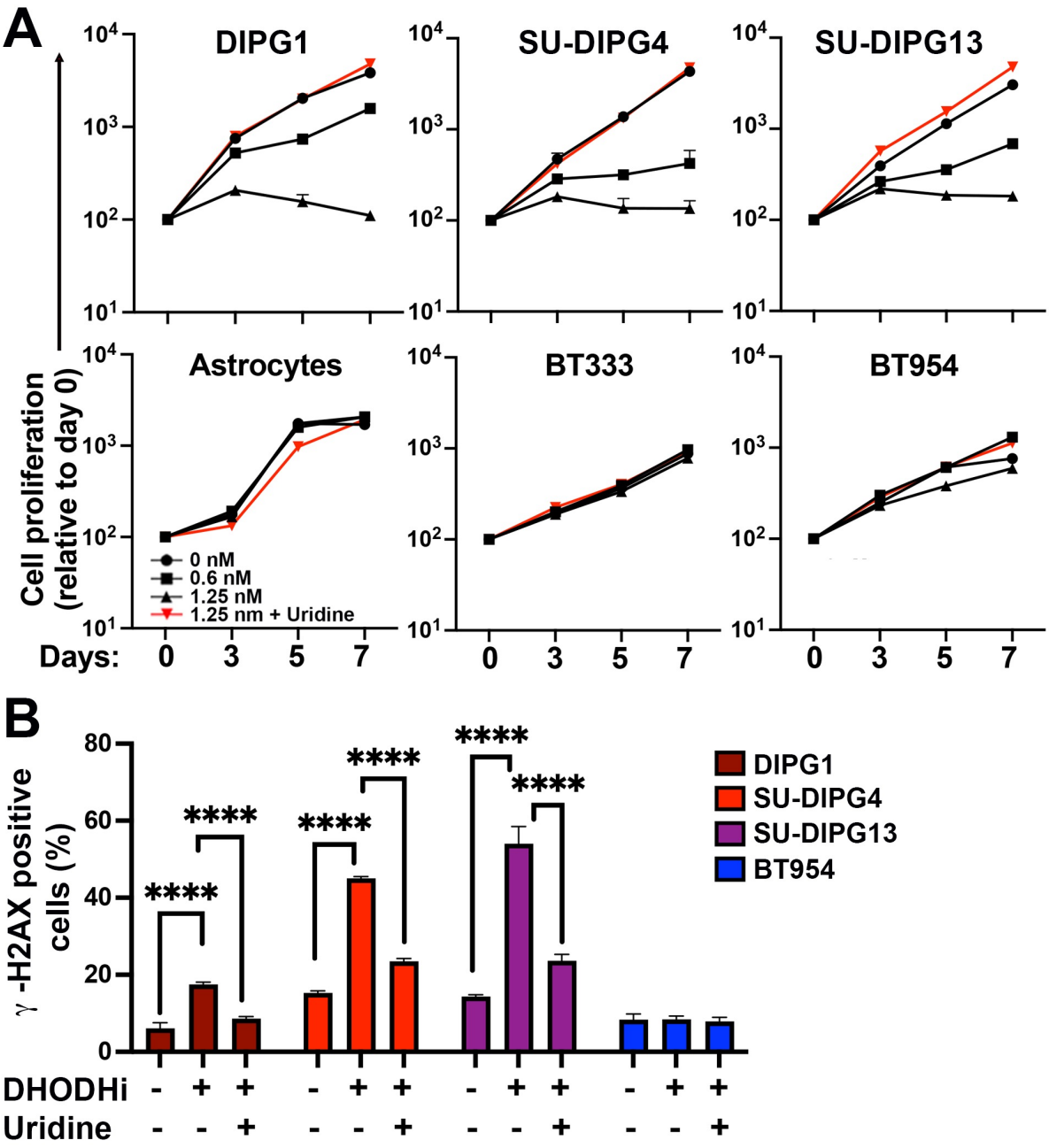

Figure 4

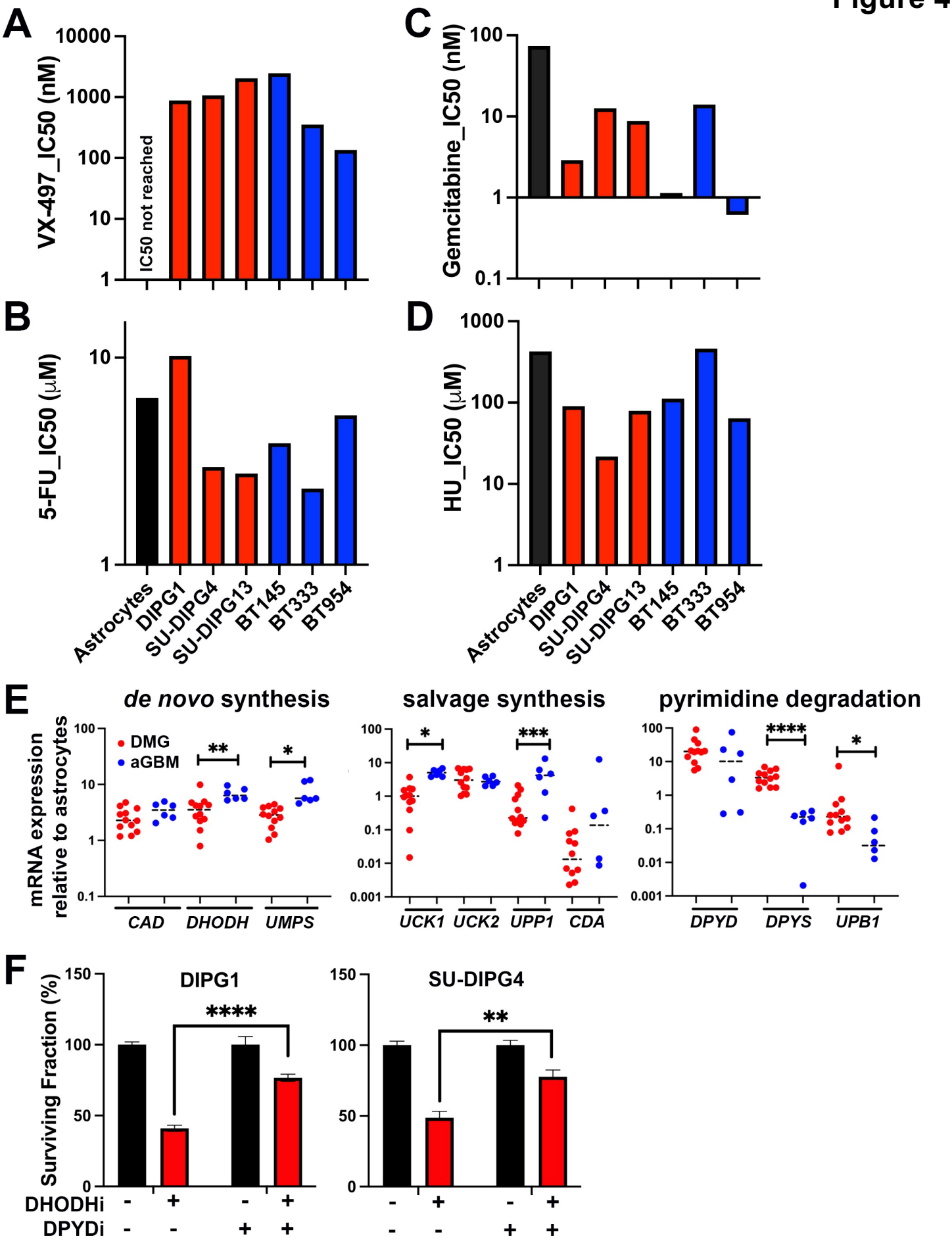

Figure 5

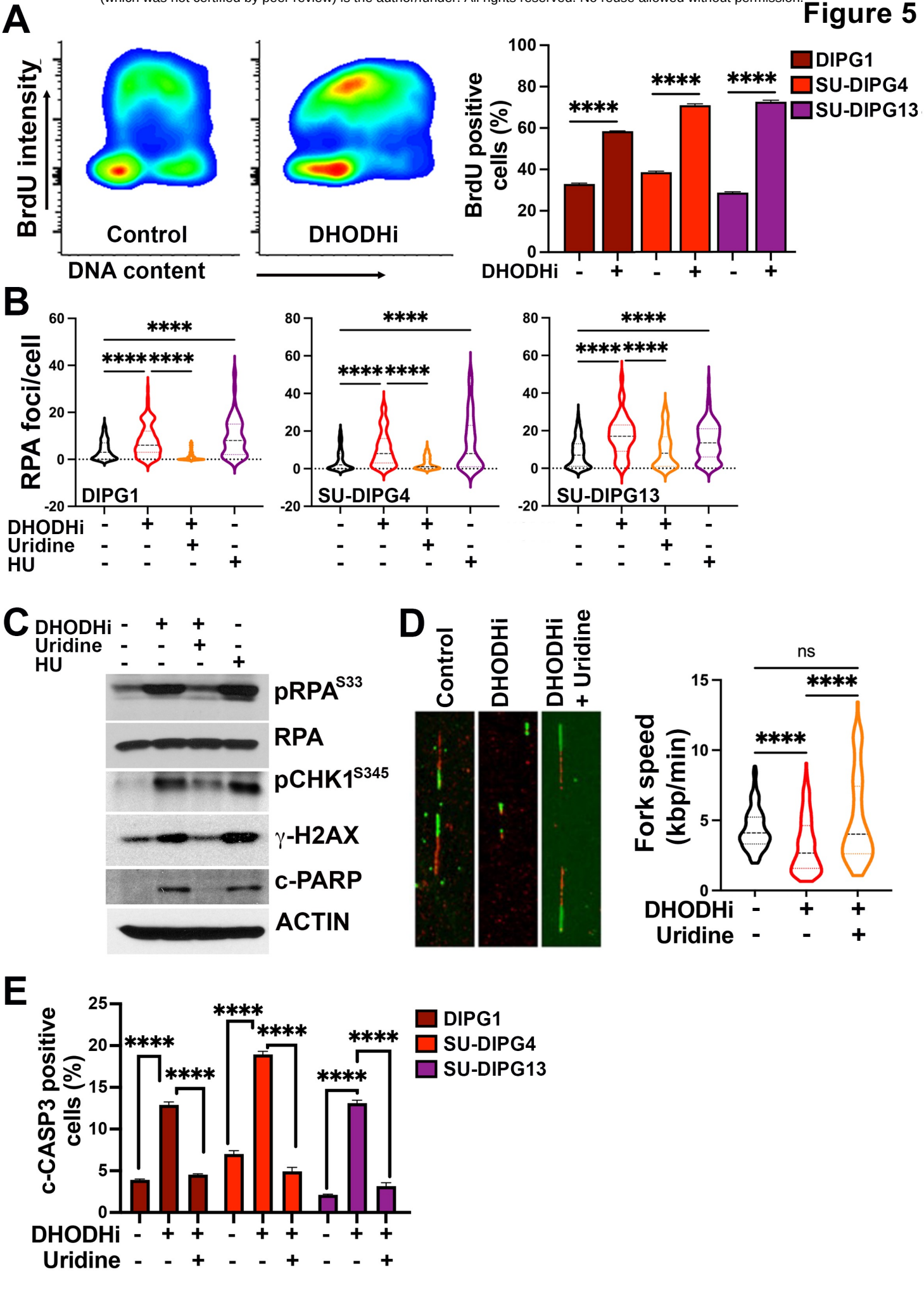

Figure 6

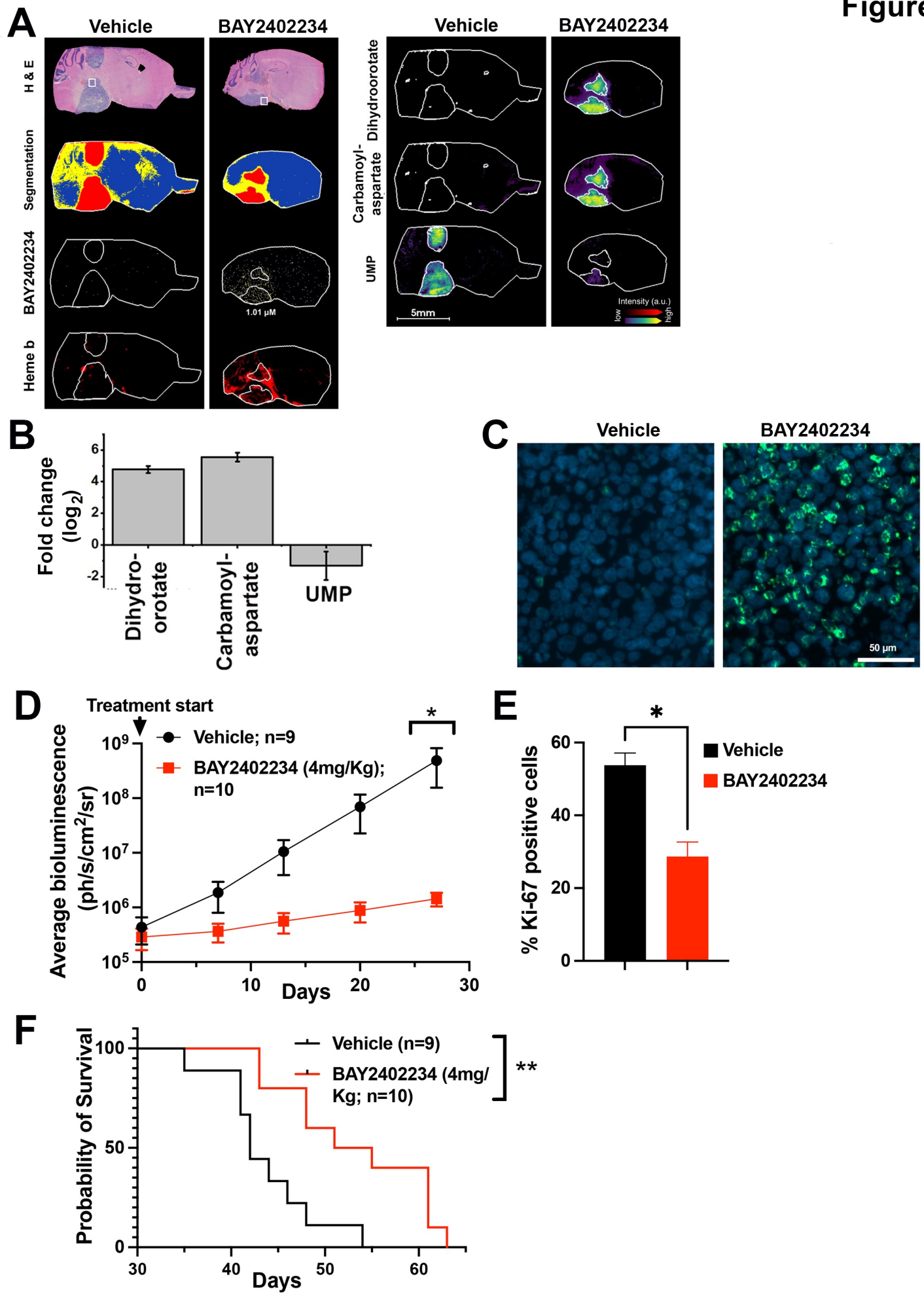

Figure 7

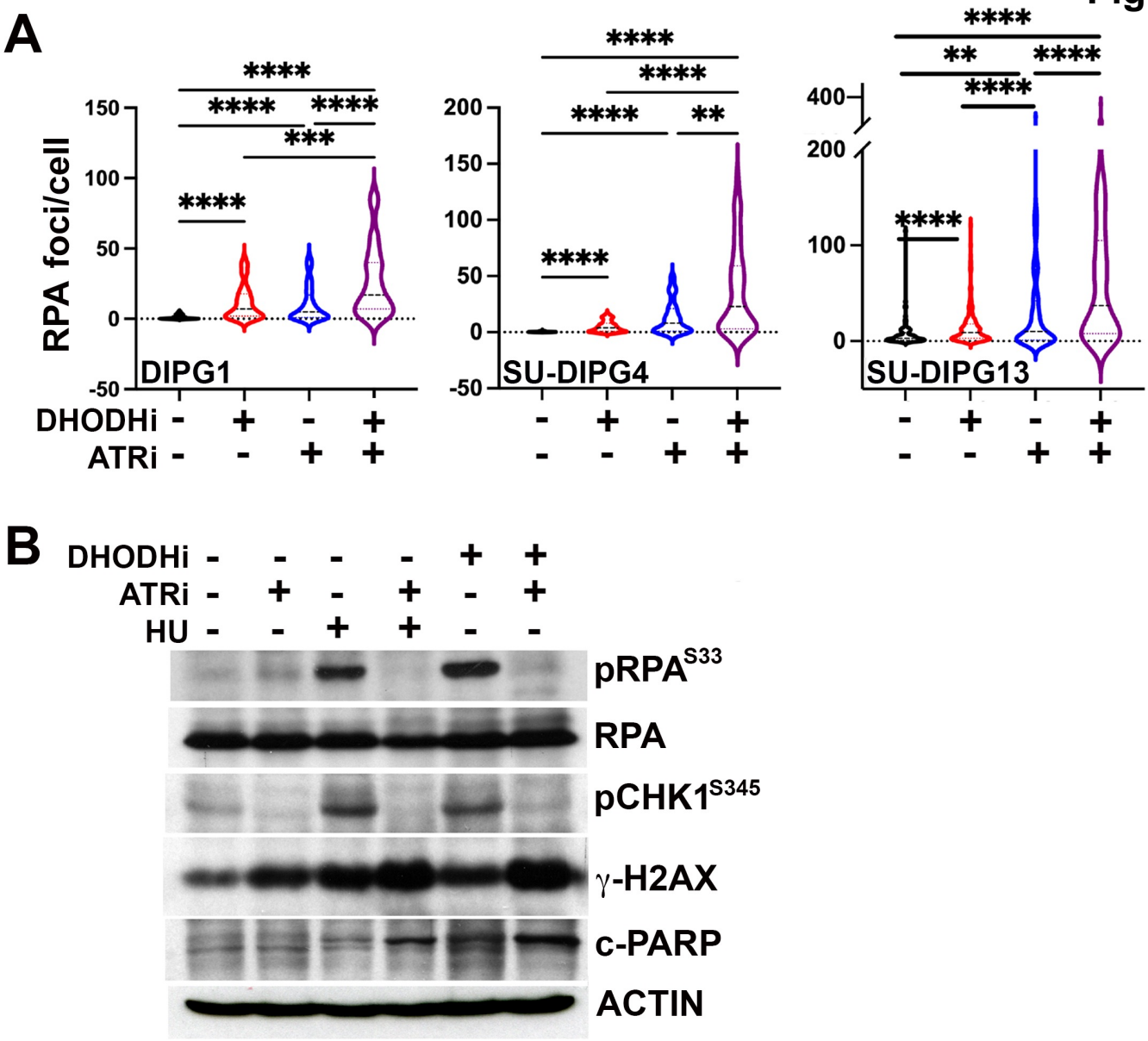

Figure 8